Monthly Notices of the ROYAL ASTRONOMICAL SOCIETY

MNRAS **514,** 2974–2993 (2022) https://doi.org/10.1093/mnras/stac1381
Advance Access publication 2022 May 18

The lively accretion disc in NGC 2992 – II. The 2019/2021 X-ray monitoring campaigns

R. Middei [1,2★] A. Marinucci [3] V. Braito [4,5] S. Bianchi [6] B. De Marco,[7] A. Luminari [1,8] G. Matt,[6] E. Nardini [9] M. Perri,[1,2] J. N. Reeves[4,5] and F. Vagnetti[8,10]

[1]*INAF – Osservatorio Astronomico di Roma, Via Frascati 33, Monte Porzio Catone, I-00078 Roma, Italy*
[2]*Space Science Data Center – ASI, Via del Politecnico s.n.c., I-00133 Roma, Italy*
[3]*ASI – Italian Space Agency, Via del Politecnico snc, I-00133 Rome, Italy*
[4]*Center for Space Science and Technology, University of Maryland Baltimore County, 1000 Hilltop Circle, Baltimore, MD 21250, USA*
[5]*INAF – Osservatorio Astronomico di Brera, Via Bianchi 46, I-23807 Merate, LC, Italy*
[6]*Dipartimento di Matematica e Fisica, Università degli Studi Roma Tre, via della Vasca Navale 84, I-00146 Roma, Italy*
[7]*Departament de Fìsica, EEBE, Universitat Politècnica de Catalunya, Av. Eduard Maristany 16, E-08019 Barcelona, Spain*
[8]*INAF – Istituto di Astrofisica e Planetologia Spaziali, Via del Fosso del Cavaliere, I-00133 Roma, Italy*
[9]*INAF – Osservatorio Astrofisico di Arcetri, Largo Enrico Fermi 5, I-50125 Firenze, Italy*
[10]*Dipartimento di Fisica, Università degli Studi di Roma 'Tor Vergata', Via della Ricerca Scientifica 1, I-00133 Roma, Italy*

Accepted 2022 May 12. Received 2022 May 11; in original form 2022 February 28

ABSTRACT

We report on the short- and long-term X-ray properties of the bright nearby Seyfert 2 galaxy NGC 2992, which was extensively observed with *Swift*, *XMM–Newton*, and *NuSTAR*. *Swift* targeted the source more than 100 times between 2019 and 2021 in the context of two monitoring campaigns. Both time-averaged and time-resolved analyses are performed, and we find that the short-to-long term spectral properties of NGC 2992 are dominated by a highly variable nuclear continuum. The source varied in the 2–10 keV energy band from 0.6 to 12 $\times$ 10^{-11} erg cm^{-2} s^{-1} during the two year long *Swift* monitoring. The fastest 2–10 keV flux change (by a factor of $\sim$ 60 per cent) occurred on a time-scale of a few hours. The overall emission spectrum of the source is consistent with a power law-like continuum ($\Gamma = 1.69 \pm 0.01$) absorbed by a constant line-of-sight column density $N_{\rm H} = (7.8 \pm 0.1) \times 10^{21}$ cm^{-2}. The reflected emission is likely due to matter with an average column density $N_{\rm H} = (9.6 \pm 2.7) \times 10^{22}$ cm^{-2}, thus NGC 2992 appears to have a globally Compton-thin circumnuclear medium. This scenario is fully supported by an independent analysis of the fractional variability and by *XMM–Newton* multiyear spectra.

Key words: galaxies: active – galaxies: Seyfert – X-rays: galaxies – X-rays: individuals (NGC 2992).

1 INTRODUCTION

Active galactic nuclei (AGNs) are extragalactic sources that emit across the whole electromagnetic spectrum. Such systems are composite and each sub-structure has its own role in shaping the emerging spectrum (see Padovani et al. 2017, for a comprehensive review). It is ubiquitously accepted that the X-ray emission originates in the very inner regions of AGNs, near the central supermassive black hole (SMBH). Accretion of matter infalling on to the SMBH is responsible for the enormous amount of optical-UV photons, a fraction of which can be further energized via inverse-Compton (Sunyaev & Titarchuk 1980) off thermal electrons (the so-called hot corona: Haardt & Maraschi 1991, 1993; Madejski et al. 1995; Zdziarski et al. 1995) up to the X-rays. The maximum energy gain for these seed photons is mainly set by the hot plasma's temperature, and, to a lower extent, by its opacity (e.g. Rybicki & Lightman 1979; Beloborodov 1999; Middei et al. 2019). In fact, the X-ray continuum in AGNs is well modelled by a power law with a high energy roll-over (e.g. Perola et al. 2002; Dadina 2007; Molina et al. 2009, 2013; Malizia et al. 2014; Fabian et al. 2015, 2017; Ricci et al. 2018; Tortosa et al. 2018). AGN X-ray spectra may show additional features due to reprocessing of the primary X-ray emission by the circumnuclear material. A fluorescence emission line from the Fe K-shell is commonly observed as the most prominent feature (e.g. Bianchi et al. 2009) and its analysis carries a wealth of information on the physics of the reflecting material. This emission line has an intrinsically narrow profile that can undergo distortions, such as broadening, due to special and general relativistic effects. In particular, the closer to the SMBH the reflectors, the more distorted (i.e. the broader) the neutral or ionized Fe line profile (e.g. Fabian et al. 1995). On the contrary, at larger distance, these effects are negligible, thus the Fe Kα shape is consistent with a narrow profile. Additionally, in the case of Compton-thick reflectors (i.e. $N_{\rm H} \gtrsim 1.5 \times 10^{24}$ cm^{-2}) the X-ray spectra show a typical emission excess around 30 keV, the so-called Compton-hump (e.g. Matt, Fabian & Ross 1993). The effect of any absorbing matter crossing our line of sight can significantly attenuate the observed number of photons, especially in the soft X-rays (e.g. Cappi et al. 1999; Awaki et al. 2000; Matt 2002; Bianchi et al. 2009; Middei et al. 2021).

The X-ray emission of AGNs is also well known to be variable in spectral shape and amplitude. Nearby Seyfert galaxies as well

★ E-mail: riccardo.middei@ssdc.asi.it

Table 1. The observation log for the *XMM–Newton* and *NuSTAR* data is presented. The *NuSTAR* exposure was simultaneously taken during the second orbit of *XMM–Newton*.

Satellite	Detector Obs.	ID Obs.	Net exposure	Start-date
XMM–Newton	pn	0840920201	92.6 ks	2019-05-07
XMM–Newton	pn	0840920301	92.8 ks	2019-05-09
NuSTAR	FPMA/B	90501623002	57.4 ks	2019-05-10

as distant quasars show a typical softer-when brighter behaviour (e.g. Sobolewska & Papadakis 2009; Serafinelli, Vagnetti & Middei 2017), where softer spectral states, characterized by a photon index $\Gamma > 2$, generally correspond to higher flux states. Variability is also commonly witnessed in terms of flux changes that occur on different time intervals. Changes from months to decades are common (e.g. Papadakis et al. 2008; Vagnetti, Turriziani & Trevese 2011; Vagnetti et al. 2016; Falocco et al. 2017; Paolillo et al. 2017) and, in the X-rays, variations are also observed down to kiloseconds time-scales (e.g. Uttley, McHardy & Papadakis 2002; Ponti et al. 2012). The origin of such a rapid variability cannot be solely ascribed to the X-ray band merely mimicking the variations of the disc optical–UV photons (Nandra 2001). Moreover, a tight relation between short time-scales variations and SMBH mass (e.g. Papadakis 2004; O'Neill et al. 2005; McHardy et al. 2006; Ponti et al. 2012) is well established.

Multi-epoch high S/N spectral and timing data provide compelling pieces of information to shed light on to the physics behind X-ray variability and its tight link with the emerging X-ray spectrum. In this context, we report on the X-ray spectral properties of NGC 2992, a nearby highly inclined spiral galaxy ($z = 0.00771$, Keel 1996) classified as a Seyfert 1.5–1.9 galaxy (Trippe et al. 2008). This source was the target of two consecutive *XMM–Newton* orbits in 2019, the second of which had a simultaneous but shorter *NuSTAR* exposure. Multiple transient Fe K emission lines between 5 and 7 keV were found, originating from several flaring sectors of the accretion disc (Marinucci et al. 2020). Moreover, variable absorption structures above 9 keV were also detected, associated with an intermittent disc wind (Luminari et al., submitted). The general trend of the source (already reported in Yaqoob et al. 2007; Shu et al. 2010; Marinucci et al. 2018), where relativistic emission lines are observed at high flux levels, was therefore confirmed. In this paper, we report on the analysis of all the Neil Gehrels Swift Observatory (hereafter Swift) data, most of which were taken in the context of two monitoring campaigns. Then, we present a detailed timing and spectral analysis of the *XMM–Newton* and *NuSTAR* 2019 observations.

2 DATA REDUCTION AND SCIENCE PRODUCTS EXTRACTION

This paper focuses on NGC 2992 observations (longer than 100 s) taken in the context of *Swift* monitoring campaigns. In the first one, *Swift-XRT* monitored NGC 2992 throughout 2019 (from March 26 to December 14), with the aim of triggering a deep, high flux observation of the source. On 2019 May 6, the triggering flux threshold was met ($F_{2-10} = 7.0 \times 10^{-11}$ erg cm^{-2} s^{-1}) and *XMM–Newton* started observing the source on 2019 May 7 for two consecutive orbits (ObsIDs: 0840920201, 0840920301). *NuSTAR* (Harrison et al. 2013) observed NGC 2992 on 2019 May 10 for ∼120 ks, simultaneously with the second *XMM–Newton* orbit. In this paper, we consider the same data set presented in Marinucci et al. (2020) and Luminari et al. (submitted) (see also Table 1) and we address the reader to these papers for details on the data reduction.

Table 2. Extraction regions properties as a function of the *XRT* observed rate.

Region's shape	Radius (inner radius) pixel	Rate cts s^{-1}
Circle	20	<0.6
Annulus	(2)	>0.6
Annulus	(3)	>1.4
Annulus	(4)	>1.7
Annulus	(5)	>2.8
Annulus	(6)	>3.2

Then, we also consider exposures obtained during a novel 2021 *Swift* monitoring aimed at keeping track of the extreme variability of NGC 2992.

The extraction of the high level science products of each *Swift–XRT* exposure resulted from an automatic process that downloads and reduces raw data taken via photon counting acquisition mode. The procedure is based on the standard pipelines *xrtpipeline* and *xrtproducts* described in Capalbi et al. (2005).[1] The regions used to extract the source and background spectra and light curves are selected taking into account any pile-up affecting that specific observation. In particular, after computing the source net count rate with *ximage*, the procedure selected a circular region or an annulus in the case of a rate <0.6 or >0.6 cts s^{-1}, respectively. Then, the inner radius of the annulus is determined on the basis of the observed count rate. In Table 2, we list the rates limits for each inner radius of the extracting annulus. The region used to extract the source always has an outer radius of 50 arcsec, regardless of its circular or annular shape. On the other hand, the background is always extracted using an annular region centred on the source. A difference of 25 pixels (∼60 arcsec) is set between the inner and outer radii of such a region. The outer radii of the source and background regions are always ∼60 arcsec apart. Spectra were then binned requiring a minimum of 5 counts per bin and were fitted adopting the Cash statistic (Cash 1979).

Finally, we relied on a similar automatic procedure to extract science products for each UVOT exposure. In particular, we checked that two regions, one circular and centred on the source (radius = 6 arcsec) and a concentric annulus (Δradius = 7 arcsec) were free of any other sources or spurious detection. The returned count rates for the UVOT filters are not corrected for Galactic nor intrinsic reddening. We notice that correcting for such effects would not modify our results, instead it would lead to a shift of the rates. Our computations showed that considering a reddening of $E(B-V) = 0.0519$ (Schlafly & Finkbeiner 2011) would decrease the rates by ∼13 or ∼30 per cent for the *V* and the *UVW2* filters, respectively.

3 TIMING PROPERTIES

The *Swift*, *XMM–Newton*, and *NuSTAR* observations provide a compelling data set to shed light on to the temporal properties of NGC 2992 at different time-scales.

3.1 Daily to yearly variations

Swift extensively observed NGC 2992. From 2006 to present days more than one hundred observations are available, and the bulk of

[1] https://swift.gsfc.nasa.gov/analysis/xrt_swguide_v1_2.pdf

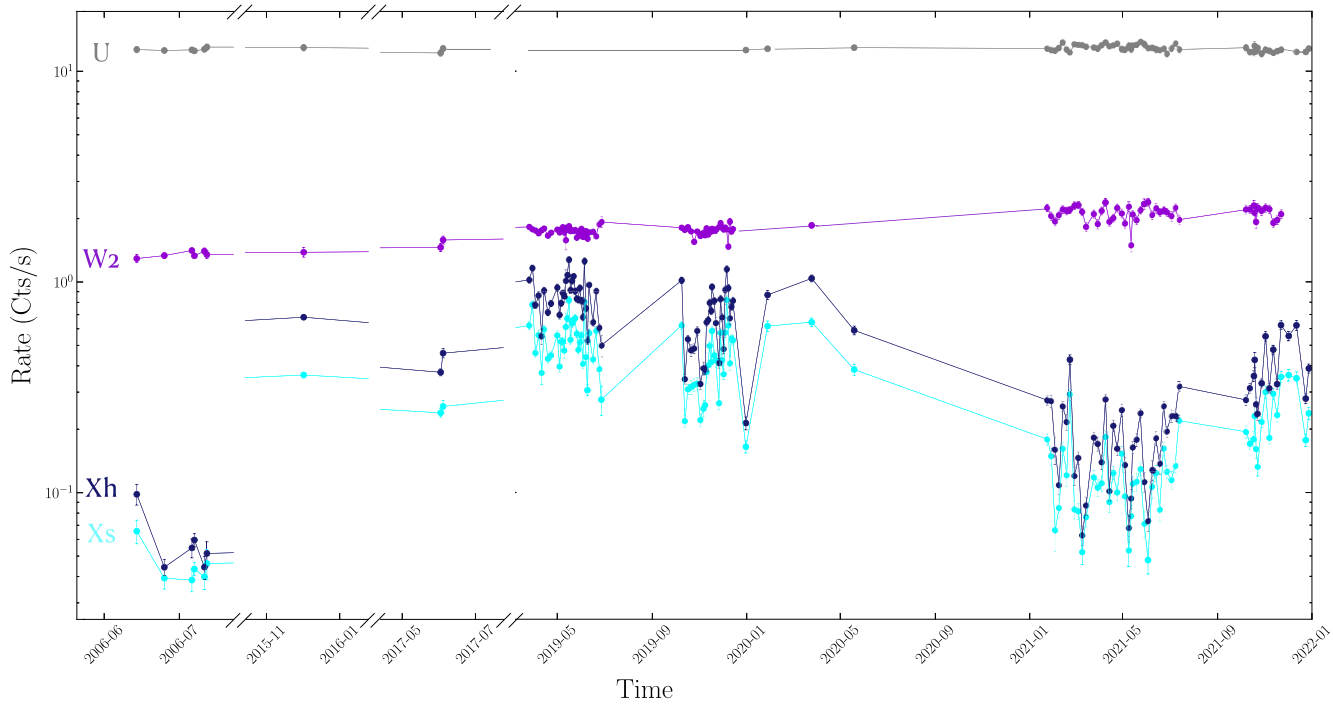

Figure 1. *Swift–XRT* and *-UVOT* light curves from the 123 observations. Remarkable variability from short to long time-scales can be observed in the X-rays, while the optical–UV light curves (not corrected for the extinction) are characterized by a more constant behaviour. *UVOT* filters are labelled in the plot while Xs and Xh account for X-rays in the 0.3–2 and 2–10 keV energy ranges. We notice that for visual purposes, each segment of the *x*-axis has a different length.

the exposures belong to two distinct monitoring campaigns, one held during 2019 from which 60–2 ks exposures were derived, and a novel one covering 2021.

Multi-epoch and multiwavelength light curves are showed in Fig. 1, where remarkable variations are observed from daily to yearly time-scales. The lowest X-ray state corresponded to the archival observations from 2006 and a maximal variation larger than a factor of 10 is found. To the fast X-ray variations correspond fairly flat optical and UV time series. Such a constant behaviour, is clearly observed in the optical filters *U* (with both *V* and *B* showing the same trend) and *UVW2*, although in this ultraviolet band we can see a marginal long-term increase. The flat shape of the optical–UV light curves for NGC 2992 can be straightforwardly accounted for by the obscured nature of this source, implying that even if the AGN may contribute, it does not dominate the emission in these bands.

The well-sampled X-ray light curves obtained from the monitoring campaigns allow us to compute the corresponding structure functions (SFs). The SF has been widely adopted in different bands of the electromagnetic spectrum (Trevese et al. 1994; de Vries et al. 2005; Bauer et al. 2009) and quantifies the amount of variability giving a measure of the mean change between two observations separated by a time-lag τ. It has been used for ensemble studies (see Vagnetti et al. 2011, 2016, for details) as well as for single AGN (e.g. Gallo et al. 2018; Laurenti et al. 2020). Different mathematical formulations for such an estimator have been proposed (e.g. Simonetti, Cordes & Heeschen 1985; di Clemente et al. 1996), and we here use the one described in section 3 of Middei et al. (2017). In Fig. 2, we show the soft (0.3–2 keV) and hard (2–10 keV) SFs for the two *Swift–XRT* campaigns. Flux changes in both bands increase with the rest-frame time-lags, $\mathrm{SF_{hard}} \sim \tau^{0.12 \pm 0.02}$ and $\mathrm{SF_{soft}} \sim \tau^{0.10 \pm 0.02}$, with these slopes being compatible with the one found from ensemble studies focusing on the average variability of AGNs ($\mathrm{SF_{ensemble}} \sim \tau^{0.121 \pm 0.004}$, Vagnetti et al. 2016). The normalizations of the SFs account for two different variability levels, the larger the variability, the higher the SF. Interestingly, larger variability is measured during 2021 corresponding to a lower flux state of the source.

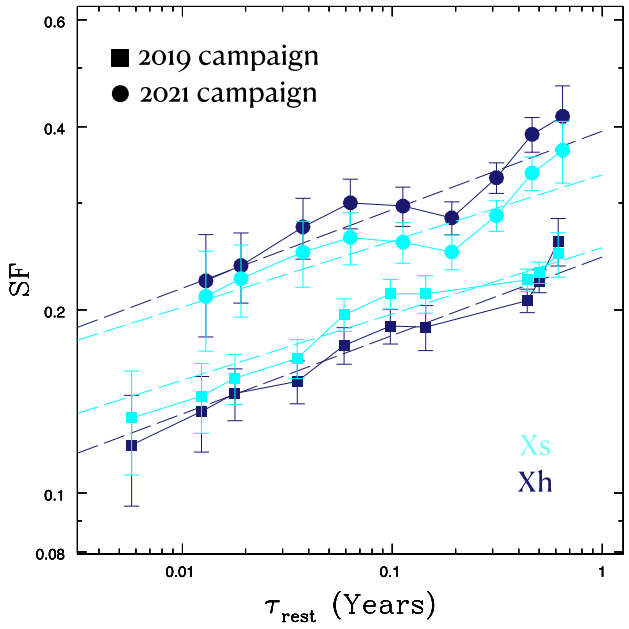

Figure 2. Structure functions for the soft and hard X-rays computed for the two monitoring campaigns. Dashed lines account for the weighted linear regression describing the SF. Light curves in 2021 were more variable than in 2019 and both the hard and soft X-rays varied of the same amount within each monitoring.

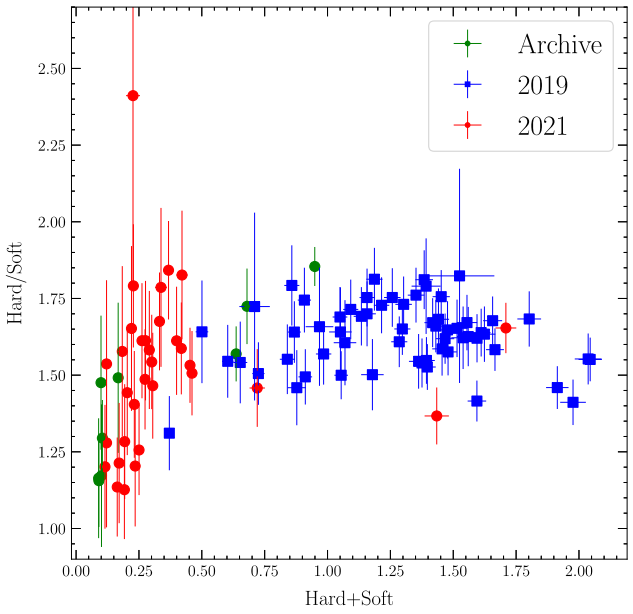

Figure 3. NGC 2992 hardness ratios as a function of the total collected counts in the 0.3–10 keV band. Different colours identify data from the 2019 (blue), 2021 (red), and those already in the archive (green).

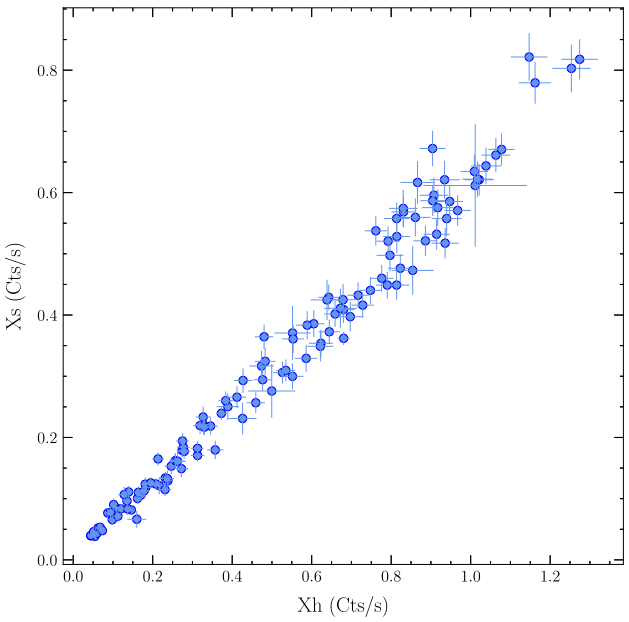

Figure 4. Correlation between soft and hard count rates (0.3–2 and 2–10 keV, respectively). This suggests that the power-law component dominates the ∼1–10 keV spectrum of NGC 2992.

We then searched for correlations possibly connected with variations in the column density of the obscurer. For this reason, we computed the ratio between the hard and soft X-rays and we studied it as a function of the total counts. In accordance with the plot in Fig. 3 no correlation holds between the hard/soft X-ray ratio and full band rate, and a marginal trend can be only observed for a full band rate below 0.5 cts s^{-1}. The lack of a noticeable trend is consistent with a fairly constant column density of the obscurer. On the other hand, the soft and hard X-rays are strongly correlated ($P_{cc} = 0.99$, $P(<r) < 0.01$ per cent), see Fig. 4, suggesting that both the soft and hard X-rays are produced by the very same spectral component.

Finally, we further stress that neither the soft nor the hard X-ray bands are correlated with the ultraviolet emission, see Fig. 5. Such a correlation has been commonly observed in samples of unobscured AGN (e.g. Edelson et al. 2002; Lusso et al. 2010; Edelson et al. 2015; Lusso & Risaliti 2017) and the lack of correlation has been associated either to an incumbent changing look process (e.g. Ricci et al. 2020, 2021; Laha et al. 2022) or to intervening absorbing matter. Due to the Seyfert 2 nature of NGC 2992, the lack of a correlation between the disc and coronal emissions can be ascribed to the pre-dominantly non-nuclear nature of the UV emission observed with *Swift–UVOT*.

We further quantified the variability properties of NGC 2992 computing the so-called fractional variability (F_{var}). This estimator (e.g. Edelson et al. 2002; Vaughan et al. 2003; Ponti et al. 2004, 2006) provides a direct measure of a light-curve variability and is defined as the square root of the normalized excess variance (e.g. Vaughan et al. 2004; Ponti et al. 2006; Matzeu et al. 2016, 2017; Alston et al. 2019; De Marco et al. 2020; Igo et al. 2020; Parker et al. 2020). To derive compatible excess variance spectra, we only considered data taken during the 2019 and 2021 monitoring campaigns. In particular, for a meaningful comparison, we need to compute the F_{var} spectra using light curves of similar length. The 2019 campaign spans a time interval of about 6 months although not performed continuously due to visibility issues. We thus divided each set of observations into subsets roughly covering an about 3 months long-time interval. We

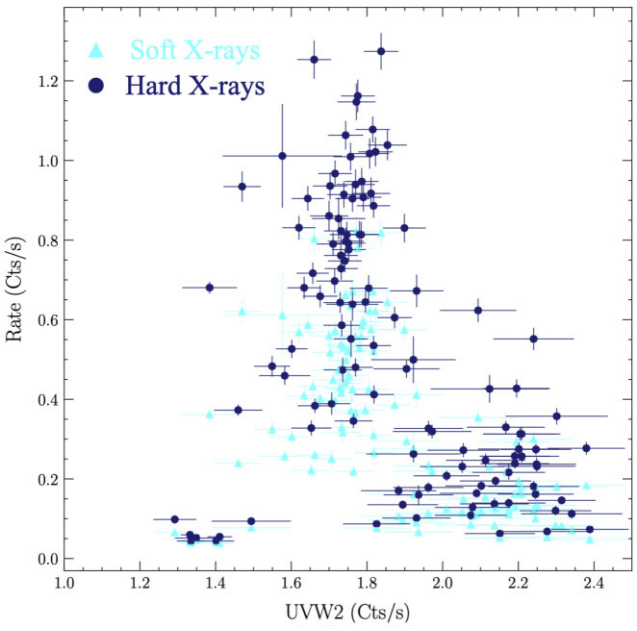

Figure 5. Lack of correlation between the X-rays and ultraviolet *UVW2* filter. Cyan triangles account for the soft X-rays while blue circles are used for the hard band. Pearson cross-correlation coefficients of $P_{cc} = -0.21$ $P(<r) = 2$ per cent and $P_{cc} = -0.19$ $P(<r) = 3$ per cent are found for the Xs versus *UVW2* and Xh versus *UVW2*, respectively.

thus ended up with five different subsamples: sample *a* (2019 March–June), sample *b* (2019 October–December), sample *c* (2021 January–March) and sample *d* (2001 April–July) and sample *e* (2021 October–December). We then computed the light curves for the samples in different energy intervals and derived the corresponding fractional variability. In Fig. 6, we show the resulting F_{var} spectra. Aside from some fluctuations above ∼7 keV, likely due to background issues

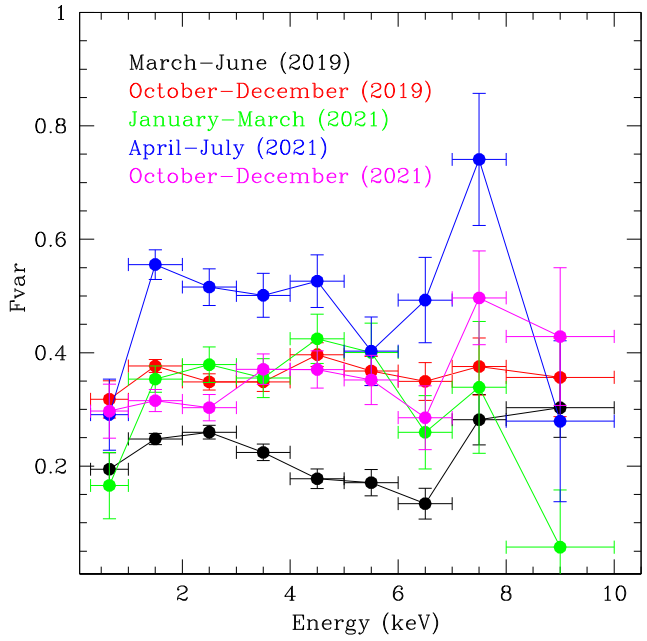

Figure 6. Fractional variability spectra derived for the five Swift's subsamples described in Section 3. Excess variance spectra clearly have different normalizations suggesting that the source varied by different amounts over monthly time-scales. Error bars only account for the Poissonian noise.

and/or low S/N, and the first energy bin that is mostly due to distant scattering, all the spectra have a fairly constant behaviour. This suggests that the variability is driven by a single variable component, which in our case is the primary continuum emission. Concerning the normalization of the spectra, we notice that the higher the $F_{\rm var}$ spectrum the lower the flux, which is in agreement with what is commonly observed in other AGNs (e.g. Barr & Mushotzky 1986; Green, McHardy & Lehto 1993; Lawrence & Papadakis 1993).

3.2 Hourly to daily changes

The two consecutive *XMM–Newton* orbits, one of which also has a simultaneous *NuSTAR* exposure, are extremely suitable for quantifying NGC 2992 variations on very short term. We started deriving the NGC 2992 light curves, see Fig. 7. The different panels, from top to bottom, account for the 0.3–1, 1–3 and 3–10, 10–79 keV bands, while the last row shows on the ratios between the soft and hard X-rays (1–3 keV/3–10 keV). The constancy of the 0.3–1 light curves is consistent with extra-nuclear, ionized emission. In orbit 1, *XMM–Newton* caught the source in a higher flux state than in orbit 2, for which data up to 79 keV are also showed. Variations during the first orbit are about a factor of 60 per cent in both the 1–3 and 3–10 keV energy bands. Such fast flux changes occur on a time-scale of ∼40 ks. On the other hand, the amount of variability in orbit 2 is reduced to a few per cent for both the soft and the hard X-ray bands. *NuSTAR*'s light curve is consistent with the 3–10 keV *XMM–Newton* time series and shows a similar amount of variability suggesting for the presence of a weak reflected component and a primary continuum still dominating this high-energy band. The hardness ratios reported in the last row of Fig. 7 are suggestive of a smooth spectral softening over the observed temporal window. In fact, ratios between the 1–3 and 3–10 keV bands increases from 0.65 at the beginning of the first orbit to ∼0.75 at the end of the second *XMM–Newton* exposure.

Thanks to the high S/N of this data set, we derived the $F_{\rm var}$ spectra of the two *XMM–Newton* exposures. We used the background subtracted light curves binned every 1000 s. The resulting variability spectra are shown in Fig. 8. The spectrum of orbit 1 has a larger normalization than orbit 2, in agreement with the light curves in Fig. 7. During orbit 1, the 1–3 keV X-rays are more variable than the hard X-rays. A moderate drop in the variability spectrum is observed around 6.4 keV, as expected for a constant Fe Kα emission. A similar drop is also observed in orbit 2, despite the ∼3 times less variable spectrum. Both spectra show a drop below ∼1 keV, as this energy range is dominated by a constant component. Finally, both spectra show an interesting variable feature around 5 keV that can possibly be associated with the transient emission line component discussed in Marinucci et al. (2020). In a recent work by Parker et al. (2020), the authors computed different tables to model $F_{\rm var}$ spectra with standard spectral fitting packages, such as *Xspec* (Arnaud 1996). Following Parker et al. (2020) and the prescriptions in the web page,[2] we tried to model our excess variance spectra. In particular, we used the following model:

Fvar_pidamp_1.fits × Fvar_pow.fits × Fvar_xildamp.fits.

The first table is based on the *Spex* photoionization model Pion (Miller et al. 2015; Mehdipour, Kaastra & Kallman 2016) and accounts for the drop in variance due to a constant photoionized emission. The model's parameters are *frac* and ξ, the ratio of the 0.5–10 keV flux of the reflection to the average log primary flux and the disc's ionization in erg cm s^{-1}. The second table reproduces the variance of a power law-like continuum changing in log(flux). Its parameters, *var* and *corr* define the variance of the logarithmic flux for the primary continuum in the 0.5–10 keV energy range and the correlation between the photon index of the power law and the variable flux. Finally, the last table is needed to account for the reduction of $F_{\rm var}$ due to unblurred reflection. In this case, the $frac_{\rm xill}$ is the ratio of the 0.5–10 keV flux of the reflection to the average power-law flux whose flux is computed in logarithm. We fitted this very same model to the two spectra finding that the first high flux orbit is well described by the model with $\chi^2 = 15$ for 13 d.o.f. and that the model works fairly well for the continuum variability of orbit 2, despite the χ^2/d.o.f. = 38/12. This poor statistics is indeed mainly due to the unaccounted excess around 5 keV and, more marginally, by scattered data above 7 keV. In Table 3 the inferred parameters for both the orbits are reported.

4 SPECTRAL PROPERTIES

As for Section 3, the multi-epoch broad-band data presented in this paper provide a compelling collection of observations suitable to perform both time-average and -resolved spectral analyses.

4.1 Mid-to-long term spectral properties

The high flux of NGC 2992 allows us to extract *XRT* spectra for each of the 123 observations presented in this paper. We thus adopted a simple model to determine the basic properties of the primary continuum and the neutral absorbing column of NGC 2992 across the years, by fitting within *Xspec* the following model:

tbabs × ztbabs × powerlaw.

[2] https://www.michaelparker.space/variance-models

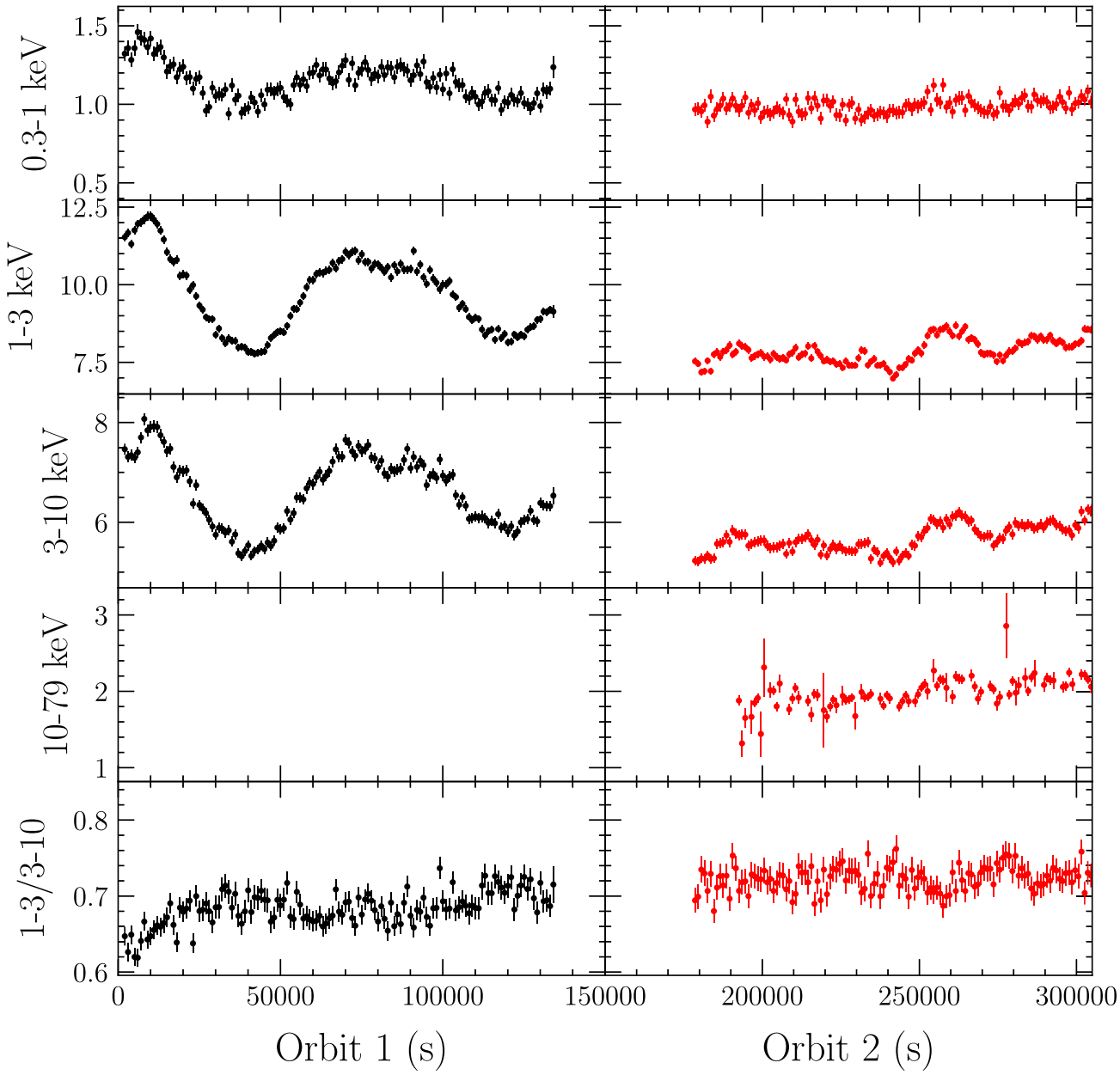

Figure 7. Background subtracted light curves in units of counts/sec are shown for *XMM–Newton* and *NuSTAR* data. Aside from the 0.3–1 keV energy band, light curves below 10 keV show remarkable changes in the first orbit and moderate flux variability in the second one. The *NuSTAR* light curve (10–79 keV) is not completely simultaneous with the second *XMM–Newton* orbit. The 3–10 keV *XMM–Newton* (orbit 2) and the 10–79 keV *NuSTAR* light curves are characterized by a similar amount of variations above 1, which suggests the primary continuum to dominate also the *NuSTAR* energy band.

The power-law models the nuclear X-ray emission and both the local and Galactic absorptions are accounted for. For each observation, we fitted the column density of the local absorber, as well as the continuum photon index and its normalization. Via this procedure we determined the best-fitting parameters shown in Fig. 9 and quoted in Table A1. Although the adopted model does not include the soft scattered component, all the spectra are well accounted for, as they all have a Cstat/d.o.f. ratio close to unity. Hard and soft X-ray fluxes show remarkable variations also down to daily time-scales, see Fig. 9. It is hard to assess whether there are spectral changes or not. As expected, in fact, the power-law photon index and the obscurer column density are strongly correlated, diluting any intrinsic spectral variability. We thus refitted all the observations keeping $N_{\rm H}$ fixed to its average value of $N_{\rm H} = 7.8 \times 10^{21}$ cm^{-2} (determined from the 123 *Swift* observations). This new attempt led to steeper values of Γ, found to have an average value of $\Gamma = 1.59 \pm 0.04$ and covering the range 1.37–1.97, see blue points in Fig. 10. Interestingly, no correlation holds between these photon indices and the total flux, so that the source does not obviously show the typical softer when brighter behaviour commonly observed in AGNs (e.g. Sobolewska & Papadakis 2009, see example in the inset of Fig. 10).

4.2 Short term spectral properties: the Fe Kα complex

We started focusing on the Fe complex of NGC 2992 testing a simple power law to the *XMM–Newton* spectra. We worked on

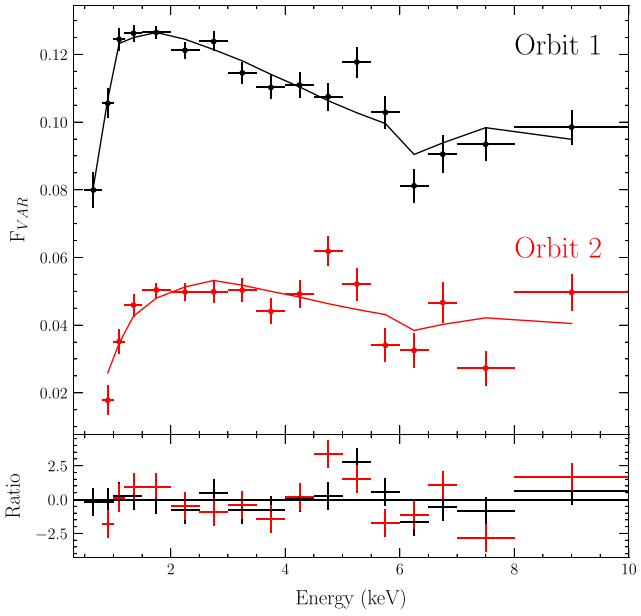

Figure 8. Fractional variability spectra of Orbits 1 and 2 derived from the background subtracted light curves. The adopted temporal binning is set to 1000 s. Interestingly, these spectra are characterized by two different amounts of variability. In particular, the higher the flux the larger the amount of variability. We notice that the second orbit spectrum lacks the 0.3–0.5 keV energy bin as it was found consistent with zero. Fitted $F_{\rm var}$ spectra are showed. In both orbits, substantial residuals can be observed around 5 keV.

the 3–8 keV energy range and we fitted the photon index and the normalization of the continuum for both orbits 1 and 2. In Fig. 11, we show zoomed spectra where modelling the sole continuum leaves prominent residuals between 6 and 7 keV. Then we added two Gaussian components with zero width to model the Fe Kα and its accompanying Fe Kβ. We assumed the lines not to change between the two orbits so that we fitted the Gaussian energy centroid and normalization for the Fe Kα. The Fe Kβ, had its energy fixed to 7.06 keV and its normalization was free to vary up to 14 per cent of the Fe Kα flux (Molendi, Bianchi & Matt 2003). Although this leads to a significant reduction in the fit statistic (χ^2/Δd.o.f. = 264/160), the data are far from being well reproduced. First of all, data between 6.4 and 7.1 keV are not yet accounted for, suggesting that the Fe Kα profile might be the superposition of different components. We then allowed the Fe Kα width to vary finding a better fit ($\Delta\chi^2 = -19$). The residuals around 6.4 keV are now accounted for. Then, we added two additional Gaussian components for the additional residuals at $\sim$6.7 and $\sim$7 keV. As for the 6.4 keV Fe Kα line, we fitted the central energy and normalization of these two Gaussians (with null width) tying the values between the orbits. In particular, one line models the Fe Ly α emission at 6.96 keV ($\Delta\chi^2/\Delta$d.o.f. = $-42/-2$) while the second accounts for the Fe He α at 6.7 keV ($\Delta\chi^2/\Delta$d.o.f. = $-47/-2$).

These steps led us to a best fit of $\chi^2 = 156$ for 155 d.o.f. and the inferred parameters are quoted in Table 4. These tests are consistent with a weakly broad Fe Kα that may be the superposition of two different components.

4.3 The *XMM–Newton/NuSTAR* 2019 observations: Time averaged spectral properties

We here derive the NGC 2992 time-average properties in the 0.5–79 keV energy range by fitting the *XMM–Newton* and the *NuSTAR* spectra. Relying on our findings in previous Section 4.2 and the phenomenological model by Marinucci et al. (2018), we built the following model in *Xspec*:

$$\text{tbabs} \times (\text{apec} + \text{Cloudy} + (\text{ztbabs} \times \text{po}) + \\ + \text{zGauss} + \text{MyTorusL} + \text{MyTorusS} + \text{zGauss} + \text{zGauss}). \quad (1)$$

4.3.1 *Soft X-rays*

The neutral Galactic and intrinsic absorption is taken into account using the *tbabs* model. The soft X-rays of type 2 AGNs are generally dominated by emission lines whose origin is a photonionized gas consistent with the narrow line region (NLR; e.g. Awaki et al. 1991; Turner et al. 1997a, b; Bianchi, Guainazzi & Chiaberge 2006; Guainazzi & Bianchi 2007; Laha et al. 2020), thus we accounted for this emission component using a grid model for *Xspec* computed with *CLOUDY* 17 (Ferland et al. 2017). This table, already presented in past studies (Bianchi et al. 2010; Marinucci et al. 2011, 2017), has two parameters: the ionising flux log U = [−2.00:4.00], with step of 0.25, and cloud column density log N_H = [19.0:23.5], with step of 0.1. Then, the *apec* model was used to reproduce thermal emission from extra-nuclear material observed with *Chandra* (Colbert et al. 2005). We fitted the temperature and the normalization for the *apec* component and the column density, the ionization and the normalization of the *Cloudy* one. However, these parameters were tied between the spectra as no variations are expected for this larger scale gas down to the investigated time-scales.

4.3.2 *Hard X-rays*

A power law reproduces the nuclear continuum while *MyTorusS* and *MyTorusL*, both additive components, model the reflected emission plus its accompanying Fe Kα, Fe Kβ fluorescent emission lines. *MyTorus* (Murphy & Yaqoob 2009; Yaqoob 2012) includes the Compton down-scattering effect and the self-consistent reflected components assuming a fixed geometry of the toroidal X-ray reprocessor, for which the covering factor of the torus corresponds to a fixed half-opening angle of 60°. Here we assumed: the medium absorbing the primary continuum and the one reflecting it to have different column densities. To set this scenario up we fitted independently the column density of ztbabs[3] and *MyTorus* tables independently i.e. using the so-called decoupled mode to allow the reflector and absorber to have different column densities. Then, we fixed the viewing angle of *MyTorusL* and *MyTorusS* to 0°, thus implementing the back scattering scenario. In the fits, the photon index of the power law was tied with those of the two *MyTorus* tables and computed for both the orbits. The normalization of the nuclear emission was computed for both orbits, similar to the one of the *MyTorus* model, which we assumed to be the same between *MyTorusL* and *MyTorusS*.

4.3.3 *Emission lines*

The 5–7 keV energy range hosts prominent features in emission and we used Gaussian lines to account for all of them except for the Fe Kα and the Fe Kβ lines, which are already included in *MyTorus*. However, in Section 4.2 we found evidence for a weakly broad Fe Kα line, thus we added a Gaussian component whose energy centroid

[3]The NGC 2992 obscurer has a column density $N_H < 10^{22}$ cm^{-2}, too low to adopt the multiplicative table *MyTorusZ* commonly used to account for absorption in the line of sight.

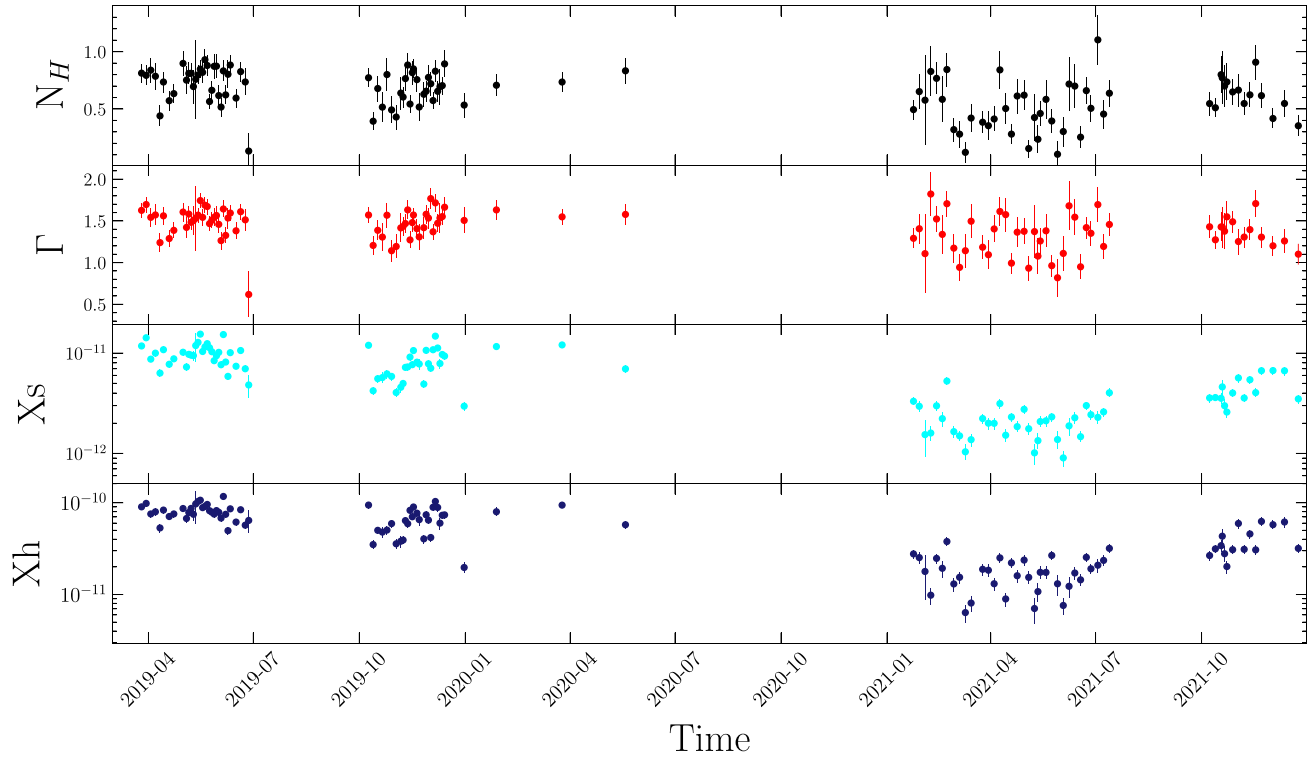

Figure 9. Best-fitting parameters derived from the analyses of the XRT exposures. The column density is in units of $\times 10^{22}$ cm^{-2} and fluxes are in units of erg cm^{-2} s^{-1}. The same results are reported in Table A1.

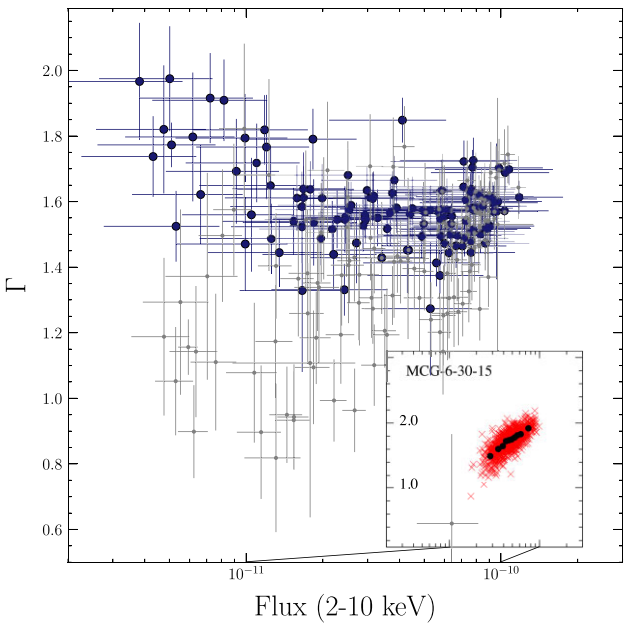

Figure 10. *XRT* photon indices as a function of the 2–10 keV flux (in units of $\times$ 10^{-11} erg cm^{-2} s^{-1}). Blue dots account for Γ values derived using a fixed absorbing column density $N_{\rm H}$ = 7.8 $\times$ 10^{21} cm^{-2}. Grey crosses, instead, represent flatter Γ values that had been derived with a free to vary $N_{\rm H}$. The inset (taken from Sobolewska & Papadakis 2009) shows MCG-6-30-15, which in contrast, does show a softer when brighter behaviour more typical of other AGN.

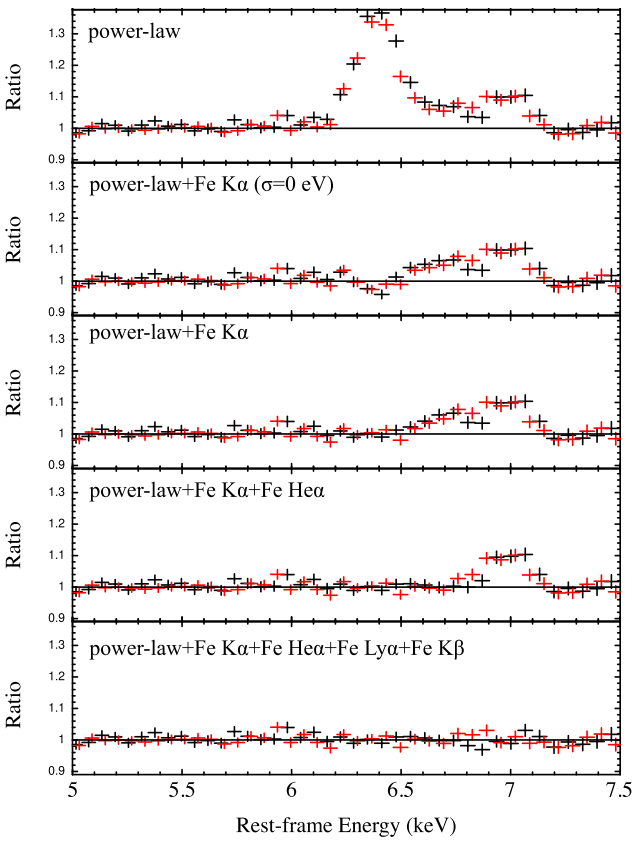

Figure 11. Zoom in the 5–7.5 keV energy band of the data to model ratios. The spectrum in black refers to orbit 1 data while the red spectrum accounts for data taken during orbit 2.

Table 3. Best-fitting parameters for the two excess variance spectra derived from the *XMM–Newton* orbits 1 and 2. The fit statistics are χ^2/d.o.f. = 15/13 and χ^2/d.o.f = 38/12 for the two spectra, respectively.

Model	Parameter	obs1	obs2
Fvar_pidamp	frac	$0.26^{+0.21}_{-0.09}$	$1.0^{+1.9}_{-0.4}$
	xi	$0.85^{+0.61}_{-0.40}$	1.6 ± 0.3
Fvar_pow	var	$0.059^{+0.002}_{-0.004}$	$0.022^{+0.005}_{-0.003}$
	corr	<0.24	<0.63
Fvar_xildamp	frac	$0.26^{+0.03}_{-0.12}$	<0.34

Table 4. Best-fitting quantities derived from the *XMM–Newton* exposures fitted in the 3–10 keV energy range. The dagger indicates that the energy centroid of the Fe Kβ was fixed.

Component	Parameter	Orbit 1	Orbit 2	Units
Tbabs	$N_{\rm H}$	1.0 ± 0.2	0.9 ± 0.2	$\times\ 10^{22}$ cm^{-2}
Pow	Γ	1.62 ± 0.03	1.66 ± 0.02	
	$N_{\rm pow}$	1.7 ± 0.1	2.1 ± 0.1	$\times\ 10^{-2}$ ph. keV^{-1} cm^2 s^{-1}
zGauss$_{\rm Fe\,K\alpha}$	E	6.38 ± 0.05		keV
	σ	46 ± 10		eV
	EW	90 ± 5		eV
	Norm	8.6 ± 0.3		$\times\ 10^{-5}$ ph. cm^{-2} s^{-1}
zGauss$_{\rm Fe\,K\beta}$†	E	7.06		keV
	EW	<20		eV
	Norm	<5.9		$\times\ 10^{-6}$ ph. cm^{-2} s^{-1}
zGauss$_{\rm FeLy\,\alpha}$	E	6.96 ± 0.01		keV
	EW	25 ± 4		eV
	Norm	2.0 ± 0.3		$\times\ 10^{-5}$ ph. cm^{-2} s^{-1}
zGauss$_{\rm Fe\,He\,\alpha}$	E	6.71 ± 0.04		keV
	EW	12 ± 3		eV
	Norm	1.2 ± 0.3		$\times\ 10^{-5}$ ph. cm^{-2} s^{-1}

was computed tying its value between the spectra and fitting its normalization in both orbits. Moreover, we fixed the centroid energy of two additional ionized Gaussians to $E = 6.7$ keV, $E = 6.96$ keV, respectively, and assumed a narrow profile ($\sigma = 0$ eV) for both of them.

These steps led to a fit statistic of χ^2/d.o.f. = 1074/731. Residuals between 3 and 5 keV suggest the photon index may not be the same for *XMM–Newton* orbit 2 and *NuSTAR* ($\Delta\Gamma \sim 0.06$). This may be either due to the non-simultaneity of the spectra or due to intercalibration issues among the detectors as also reported for other observations (e.g. Porquet et al. 2018; Laha & Ghosh 2021). Allowing for different Γ values for *XMM–Newton* and *NuSTAR* in orbit 2 yields a better fit statistic of χ^2/d.o.f. = 980/730 (see Fig. 12), and we report in Table 5 the corresponding best-fitting parameters.

In accordance with the light curves, the first orbit NGC 2992 showed a higher flux than in orbit 2, accompanied by a spectral shape characterized by a similar photon index of $\Gamma = 1.68 \pm 0.01$ and absorbing column density of $N_{\rm H} = 7.8 \pm 0.2 \times 10^{21}$ cm^{-2}. In a similar fashion, the reflected emission has a compatible flux between the two observations and a rather constant column density $N_{\rm H} \sim 9.6 \times 10^{22}$ cm^{-2} for the scattered component out of the line of sight. The presence of Compton-thin matter both along the line of sight and out of the line of sight implies the overall emission spectrum of NGC 2992 being globally Compton-thin. Only upper limits were found for the variable Fe Kα red tail while the Fe XXV He α and Fe XXVI Ly α are well constrained in both orbits. Despite the fairly acceptable statistics, the model well reproduces the *XMM–Newton* and *NuSTAR* spectra as the high χ^2 is mainly due to residuals between 1 and 2 keV likely resulting from calibration issues.

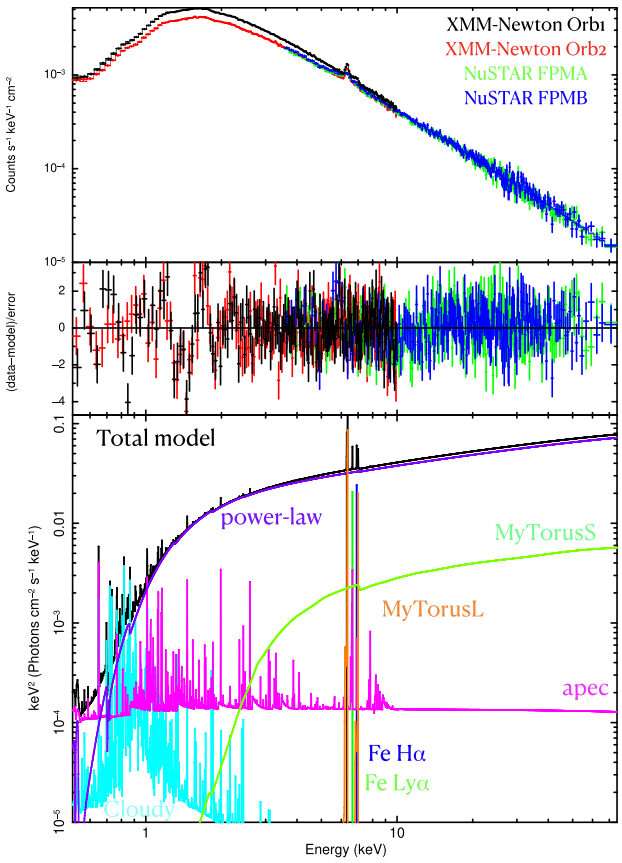

Figure 12. Best fit for the two *XMM–Newton* orbits and the accompanying *NuSTAR* data. The inferred parameters are reported in Table 5. The model components shown and labelled in the bottom panel are those derived for the simultaneous *XMM–Newton–NuSTAR* data only.

4.4 High energy cut-off

The broad-band coverage provided by a simultaneous *XMM–Newton–NuSTAR* exposure is extremely suitable to investigate for the high energy roll-over of the nuclear continuum emission, which provides direct clues on the physical properties of the hot corona. For this reason, here we focus on data belonging to *XMM–Newton* orbit 2 and those from its accompanying *NuSTAR* observation.

In Section 4.3, we found the overall emission spectrum of NGC 2992 to be globally Compton thin. We thus further investigate the properties of the X-ray emission in NGC 2992 replacing *MyTorus* with the *Borus* model (Baloković et al. 2018; Baloković, García & Cabral 2019; Baloković et al. 2021). In this model, in fact, the high energy cut-off of the primary continuum is set as a free parameter and is not fixed to 300 keV. In this model, a homogeneous spherical scattering medium is considered to surround the central X-ray source. Except for Fe, whose relative abundance ($A_{\rm Fe}$) can be derived, a solar abundance is considered. We therefore modelled the simultaneous *XMM–Newton/NuSTAR* orbit 2 replacing the *MyTorus* tables with the *Borus* one (borus02_v170323a.fits) ending up with the model:

$$\begin{aligned}&{\rm tbabs_G} \times ({\rm apec} + {\rm Cloudy} + ({\rm tbabs_z} \times {\rm cutoffpl}) + \\ &+ {\rm Borus} + {\rm zGauss} + {\rm zGauss} + {\rm zGauss}). \end{aligned} \quad (2)$$

We fit *XMM–Newton* orbit 2 and NuSTAR data computing the *Borus* normalization and column density. We assumed the cut-off power law and *Borus* to have the same primary photon index, high energy

Table 5. Best-fitting values for the fit with statistic $\chi^2 = 980$ for 730 d.o.f. as derived in accordance with Section 4.2. The † is used to identify those parameters that have been computed tying the values among the orbits.

Component	Parameter	Orbit 1	Orbit 2 + NuSTAR	Units
Cloudy†	log U	2.66 ± 0.01		
	log $N_{\rm H}$	20.4 ± 0.1		
	N	6.1 ± 0.2		$\times\ 10^{-16}$
Apec†	kT	0.68 ± 0.02		
	Norm	1.0 ± 0.4		$\times\ 10^{-4}$
ztbabs	$N_{\rm H}$	0.79 ± 0.01	0.78 ± 0.01	$\times\ 10^{22}$ cm^{-2}
Pow	Γ	1.70 ± 0.01	1.68 ± 0.01	
	$N_{\rm pow}$	2.1 ± 0.2	1.6 ± 0.1	$\times\ 10^{-2}$ ph. keV^{-1} cm^2 s^{-1}
zGauss†	E	6.33 ± 0.05		keV
	EW	25^{+31}_{-10}	15^{+16}_{-9}	eV
	N	$1.9^{+2.2}_{-0.7}$	$1.6^{+1.1}_{-0.6}$	$\times\ 10^{-5}$ ph. cm^{-2} s^{-1}
MyTorusS	$N_{\rm H}$	9.2 ± 3.1	10 ± 2.4	$\times\ 10^{22}$cm^{-2}
	N	6.4 ± 2.0	5.2 ± 0.9	$\times\ 10^{-2}$ ph. keV^{-1} cm^2 s^{-1}
zGauss	$N_{6.96\ \rm keV}$	1.15 ± 0.04	0.9 ± 0.3	$\times\ 10^{-5}$ ph. cm^{-2} s^{-1}
zGauss	$N_{6.70\ \rm keV}$	1.40 ± 0.04	1.0 ± 0.3	$\times\ 10^{-5}$ ph. cm^{-2} s^{-1}
	$F_{0.5-2\ \rm keV}$	1.3 ± 0.2	1.1 ± 0.3	$\times\ 10^{-11}$ erg cm^{-2} s^{-1}
	$F_{2-10\ \rm keV}$	8.6 ± 0.1	7.5 ± 0.01	$\times\ 10^{-11}$ erg cm^{-2} s^{-1}

cut-off and normalization, hence we tied these parameters between the two models. The iron abundance was set to 1.

These simple steps led to a best fit of χ^2/d.o.f. = 687/563. Based on this model, the primary continuum emission of NGC 2992 has a slope of $\Gamma = 1.67 \pm 0.01$ and is absorbed by a column of $N_{\rm H} = (7.8 \pm 0.1) \times 10^{21}$ cm^{-2}. A lower limit for the high energy cut-off is found, $E_{\rm c} > 390$ keV, and the reflected emission is due to matter with $N_{\rm H} = (8.7 \pm 0.4) \times 10^{22}$ cm^{-2}. *Borus* also allows for a Comptonised continuum via the table *borus11_v190815a.fits*. We thus refitted the spectra adopting this novel table, substituting the cut-off power law by *nthcomp* (Zdziarski, Johnson & Magdziarz 1996; Życki, Done & Smith 1999) and tying the equivalent parameters between the two models. The model yielded a best fit of $\chi^2 = 686$ for 563 d.o.f. fully compatible with the previous one. Aside from a slightly steeper photon index ($\Gamma = 1.71 \pm 0.01$), a very high temperature of kT > 115 keV is implied and, under the assumption of a spherical corona, we derived an optical depth of $\tau < 1.2$. All the other parameters are consistent with the previous fit.

It is worth noticing that irrespectively from the model adopted, matter on/out of the line of sight has a column density smaller than the threshold for Compton-thick regime, this further confirming the emission spectrum of NGC 2992 to be globally Compton-thin.

5 VERY SHORT TERM SPECTRAL PROPERTIES

Marinucci et al. (2020) presented a time-resolved spectral analysis on 50 *EPIC-pn* slices (each ∼5 ks long). We here perform a further step re-analysing the same spectral chunks adding *NuSTAR* when available and replacing the phenomenological model presented in that paper with the best-fitting model discussed in Section 4.3. In particular, we seek for short variations of the continuum shape and normalization and its associated reflected component *MyTorusS*.

For each spectral chunk, we computed the photon index and the normalization of the continuum and, for the reflected component *MyTorus*, the column density and its normalization. In Marinucci et al. (2020), the presence of the Fe He α and Fe Lyα plus a variable red component has already been presented. To account for these features, we relied on the best-fitting model presented in that paper, but we recalculated the line normalizations as we have adopted a different continuum. Finally, for the *apec* and CLOUDY components considered the best-fitting values from Table 5, but allowed to vary their normalizations.

This fitting strategy provided a good representation for all the spectral slices, see Figs A1 and A2, and allowed us to infer the best-fitting parameters in Table A2. The same quantities are also shown in Fig. 13. From this figure, we notice that prominent flux variability of the soft and hard X-ray bands does not correlate with the absorbing column density, nor the source spectral shape, suggesting that the variability in NGC 2992 is intrinsic, or in other words, it is not driven by absorption changes. We also notice that both Γ and $N_{\rm H}$ had a fairly constant value during the observation and, besides a few exceptions, they are consistent with the average values of $\Gamma = 1.68 \pm 0.03$ and $N_{\rm H} = (7.7 \pm 0.2) \times 10^{21}$ cm^{-2}, respectively. In a similar fashion, the reflected component does not vary significantly between the exposures and is consistent with originating from Compton-thin material, where $N_{\rm H} = (6.3 \pm 2.4) \times 10^{22}$ cm^{-2}.

6 DISCUSSION AND CONCLUSIONS

NGC 2992 is a X-ray bright AGN that has been repeatedly observed by all the major X-ray facilities. The hallmark of its emission is the significant variability of the primary continuum that has now an ∼40 yr long light curve, see Fig. 14. In this paper, we focused on data taken after 2019 analysing a rich collection of X-ray observations of NGC 2992. In particular, by exploiting *Swift*, *XMM–Newton*, and *NuSTAR* data, we derived both temporal and spectral properties for this source over different time-scales, from hours to years. In the following, we summarize and discuss our main findings.

6.1 Timing properties

The light curves show the source to vary at significant levels. Daily to yearly variations can be observed in Fig. 1, where the 2–10 keV flux varied by up to a factor of ∼5 increasing up to a factor of ∼10 when extending the observing time interval to ∼1 yr. This factor further increases comparing archival observations taken during 2006 with those of 2019. Remarkable flux changes of about ∼60 per cent

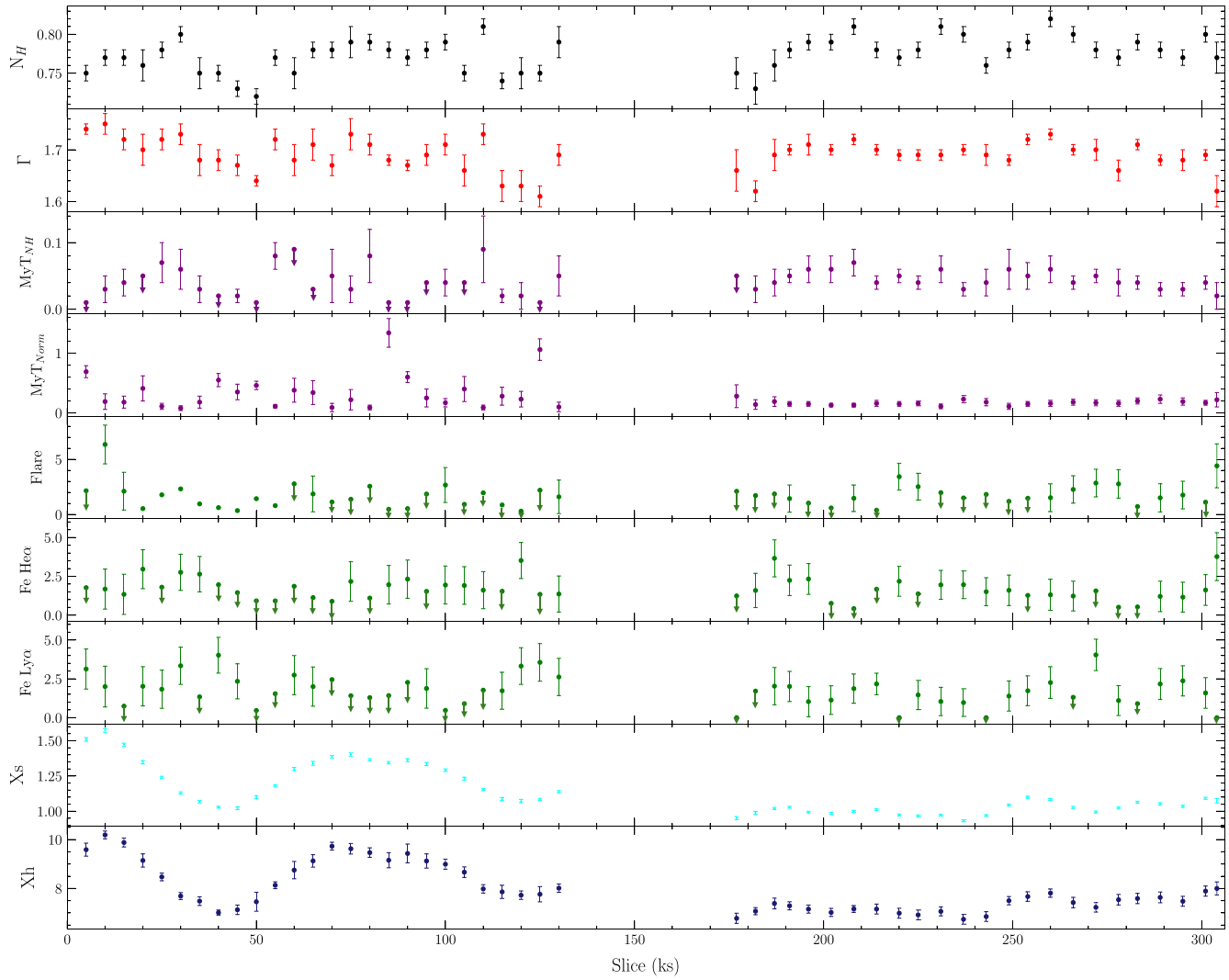

Figure 13. Best fit for the two *XMM–Newton* orbits and the accompanying *NuSTAR* data. Xs and Xh account for the soft (0.5–2 keV) and hard (2–10 keV) fluxes, respectively. Units and multiplicative factors for the parameters are given in Table A2.

were observed down to kilo second time-scales in the 1–3 keV and 3–10 keV bands, see Fig. 7. Interestingly, the larger variations were only observed in the first *XMM–Newton* orbit as, in the second one, smaller amplitude changes were observed. Aside from counts below 1 keV dominated by a constant ionized component likely emerging from the narrow line region, the variations in the soft and hard X-rays are of a similar amount. Further evidence of this comes from the consistent shapes of soft and hard SFs in Fig. 2. The lack of a correlation between the hardness ratios and the total flux in Fig. 3 allows us to rule out fast obscuration events to cause the variability which is, instead, intrinsic to the continuum emission dominating the 1–10 keV energy range, see Fig. 4.

The two *Swift* monitoring periods also revealed that the source underwent two different variability levels, see Figs 2 and 6, where the lower flux state correspond to larger variations. On the other hand, when comparing the excess variance spectra derived from *XMM–Newton*, the opposite trend is observed. In fact, the exposure with larger flux is also the more variable, see Fig. 8. The former trend has been explained invoking the presence of N randomly flaring sub-units (e.g. Nandra et al. 1997; Almaini et al. 2000), and, although it matches the flux changes for the NGC 2992 SFs and in the Fvar spectra (see Figs 2 and 6), we notice that lognormal flux distribution commonly observed in AGN strongly limits the possible number of uncorrelated active regions (Uttley, McHardy & Vaughan 2005).

Finally, the high S/N allowed us to fit the excess variance spectra following the prescriptions by Parker et al. (2020). We successfully tested on our spectra a simple variability model due to the primary continuum with a damping in the Fe Kα and in the soft X-ray regions due to the constancy of the reflected and scattered emission. The spectra of both orbits are accounted fairly well by the model. Interestingly, a strong excess around 5 keV is observed in both observations and it is stronger in orbit 2, in agreement with the variable red flaring emission component reported in Marinucci et al. (2020). From the fit, we found the variance of power-law flux in logarithmic scale to be ∼3 times larger in orbit 1 with respect to orbit 2. Moreover, this fit agrees with the nuclear X-rays to dominate the X-ray emission of NGC 2992.

6.2 Spectral properties

The main component shaping the X-ray emission of NGC 2992 is the absorbed primary continuum. The time-average analysis of the

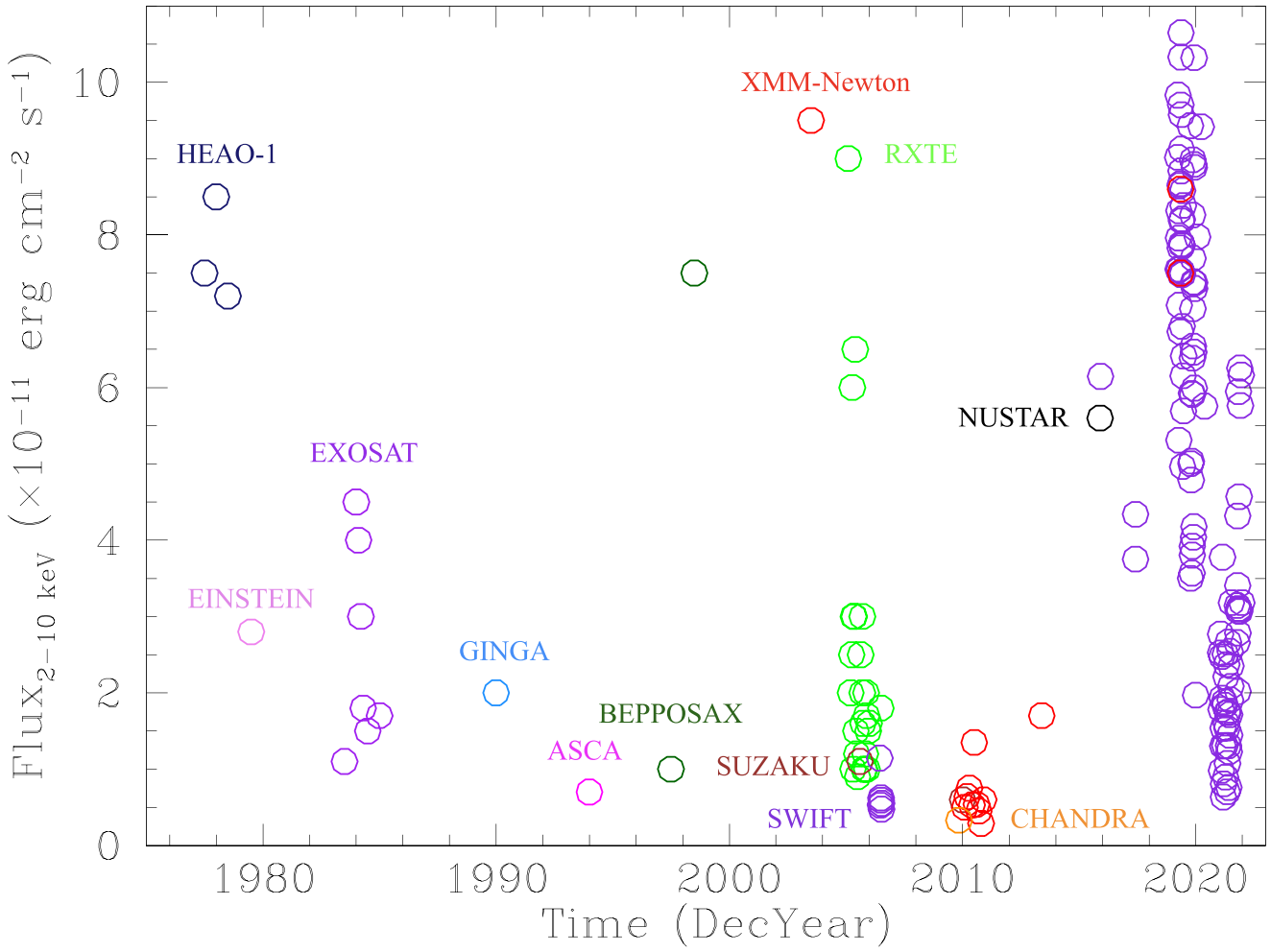

Figure 14. The historical 2–10 keV light curve of NGC 2992 as observed with various X-ray satellites. We address the reader to the paper by Yaqoob et al. (2007) and references therein, for details on data taken before 2008. Data collected after 2008 were presented in Marinucci et al. (2018, 2020) and this paper. The 2–10 keV flux derived using *NuSTAR* data taken in 2019 is consistent with the one derived from *XMM–Newton* orbit 2, thus we did not included it in this plot.

two *XMM–Newton* orbits and the *NuSTAR* exposure were consistent with a fairly hard power law ($\Gamma \sim 1.7$) and a line of sight absorbing column density of $N_{\rm H} \sim 8 \times 10^{21}$ cm^{-2}, see Table 5 and Fig. 12. Our findings are consistent with those based on *XMM–Newton* and *Suzaku* data presented in Laha et al. (2020). Moreover, these parameters are fully consistent with those derived on the same data, but via a time-resolved analysis, (see Table A2 and Fig. 13) and also with the values inferred from each of the 123 *Swift* snapshots, Table A1 and Fig. 9. Seeking for the presence of a high energy cut-off we found $E_{\rm cut} > 390$ keV. This value is significantly high, especially when compared with the median values for the high-energy cut-off of 240 and 340 keV as found for a sample of obscured AGN by Baloković et al. (2021). The peculiar properties of the NGC 2992 hot corona are further confirmed when testing a Comptonization continuum where we derive an electron temperature kT $>$ 115 keV and an opacity $\tau <$ 1.2. The comparison with the coronal properties measured by Middei et al. (2019) reveals the corona in NGC 2992 to be rather extreme, as its properties are compatible only with those of NGC 5506 (Matt et al. 2015). On theoretical grounds, the electron temperature and opacity of the hot corona are responsible for the observed photon index and high energy cut-off, however, despite the large changes in the X-ray flux the spectral properties of the source remain rather constant. The high temperature of the hot plasma in NGC 2992 can possibly explain such a decoupled variability. In accordance with fig. 6 in Middei et al. (2019) (where iso-Γ and iso-$E_{\rm cut\text{-}off}$ curves are drawn on the opacity–electron temperature parameter space), to observe a $\Delta\Gamma = 0.2$ we need to increase the temperature assuming the coronal opacity not to vary. This increase depends on the actual coronal temperature: if we consider kT $=$ 115 keV, consistent with what found in NGC 2992, and kT $=$ 50 keV (in agreement with the average temperature of the hot coronae studied in Middei et al. 2019), from $\Gamma = 1.7$ to $\Gamma = 1.5$ (1.9) we need to increase(decrease) the temperature by a factor of 35 per cent (25 per cent) or 20 per cent (10 per cent), respectively. Another possible explanation for the decoupled amplitude-spectral variations is discussed in a recent paper (Fernandez et al. 2022) where the authors suggest a bulk variation of the Comptonizing plasma. For instance, magnetic reconnection events occurring in the close surroundings of the disc may alter the hot plasma (e.g. Poutanen & Fabian 1999; de Gouveia Dal Pino, Piovezan & Kadowaki 2010). A flare of the hot corona would then boost the number of disc photons affecting the X-ray luminosity but not the spectral shape of the X-ray emission.

Distant reflection off an obscuring torus ($(N_{\rm H} = 9.6 \pm 2.7) \times 10^{22}$ cm^{-2}) accounts for the small spectral curvature in the hard X-rays and its associated narrow Fe Kα emission line at 6.4 keV. The reflected spectrum and the Fe Kα have a constant behaviour both on hourly and yearly time-scales. In fact, no correlation between the *MyTorus*

tables and the primary continuum was found and can be ascribed to reflection from cold, distant material, likely the obscuring torus itself. However, the modest broadening of the Fe Kα fluorescence line supports the presence of an additional weak (EW$\sim$20 eV) component contributing to the whole flux of this emission feature. This second Fe Kα emission component is likely emerging from matter closer with respect to the molecular torus, e.g. the BLR (e.g. Marinucci et al. 2018) and may explain the variable emission signature found by Guolo et al. (2021). We also notice that the Kα flux varied by about a factor of 4 compared to the low flux observation in Marinucci et al. (2018). Moreover it would agree with the findings by Ghosh & Pal (2021) that showed the flux of the Fe Kα emission line to follow the changes of the primary continuum on yearly time-scales. Finally, the 2019 does not require a Fe Kα emission line as broad as the one found in the 2003 *XMM–Newton* observation (e.g. Nandra et al. 1997; Brenneman & Reynolds 2009; Shu et al. 2010). In the time-resolved analysis, the adoption of a single narrow component accounting for this variable fraction of the Fe Kα flux is not required by the data, as *MyTorus* already provides a good representation of the Fe Kα on 5 ks time-scales. Finally, transient emission lines have recurrently been observed during the two *XMM–Newton* orbits, see Fig. 13, and we address the reader to Marinucci et al. (2020) for details.

NGC 2992 has been observed at different flux levels (e.g. Fig. 14) and in Marinucci et al. (2018) a detailed analysis of *XMM–Newton* exposures of this object is presented. In order to provide an holistic view of the spectral properties of the central engine in NGC 2992, we tested our 2019 best-fitting model (model 1 presented in Section 4.3) on the exposures where the source was found in its lowest and highest states. In particular, we considered the *XMM–Newton* archival observations taken on 2003-05-19 and 2010-11-28 (Obs.IDs. 0147920301[4] and 0654910901, respectively). We thus reproduced them directly adopting the best-fitting model found for orbit 2 and show it in Fig. 12. We accounted for the different flux states computing the normalization of the primary emission, its associated reflected component, and the one of the *apec* and *Cloudy* tables. All the other parameters have been kept fixed to their corresponding best-fitting values already quoted in Table 5. Moreover, to account for the broad emission line found required by the 2003 data, we added a Gaussian component whose width was kept fixed to $\sigma = 400$ eV, in accordance with what literature papers (e.g. Nandra et al. 1997; Shu et al. 2010). This basic procedure led us to the fits shown in Fig. 15, with statistics of χ^2/d.o.f. = 218/170 and χ^2/d.o.f. = 181/140. In the high flux level, ($F_{2-10\,\mathrm{keV}} = (9.5 \pm 0.1) \times 10^{-11}$ erg cm^{-2} s^{-1}), the normalization of the power law is $\mathrm{Norm_{po}} = (3.00 \pm 0.01) \times 10^{-2}$ ph. keV^{-1} cm^2 s^{-1}, about twice of what found in 2019 while the amount of reflected flux is fully consistent with what found in 2019 as we obtained $\mathrm{Norm_{MyTorus}} = (9.7 \pm 3.7) \times 10^{-2}$ ph. keV^{-1} cm^2 s^{-1}. On the other hand, in the 2010 low flux level exposure ($F_{2-10\,\mathrm{keV}} = (2.9 \pm 0.2) \times 10^{-12}$ erg cm^{-2} s^{-1}), we found the power-law normalization to be $\mathrm{Norm_{po}} = (4.7 \pm 0.2) \times 10^{-4}$ ph. keV^{-1} cm^2 s^{-1} about 20–30 times lower than in 2019. The normalization of the reflected component modelled using *MyTorus* is $\mathrm{Norm_{MyTorus}} = (9.5 \pm 1.2) \times 10^{-3}$ ph. keV^{-1} cm^2 s^{-1}, a factor of $\sim$10 less than in 2019. Therefore, on very long time-scales and during a prolonged low state of the source in 2010, the strength of the reflector appears to respond to the continuum. However, the smaller value of the reflected component found in 2010 can be explained by the torus reflecting the primary continuum of NGC 2992 during a low flux state. Observing the light curves in Fig. 1, before 2010 NGC 2992 was observed in a very low flux state, even lower than the one in 2021. Such a long-term adjustment suggests that reflected spectrum emerges far from the central engine. Finally, in accordance with previous studies, the Fe Kα emission line of NGC 2992 has an unresolved component correlating with the primary flux and emerging from the broad line region. However, the current *MyTorus*-based model accounts for whole Fe Kα flux (see residuals in Fig. 15) and data do not require any additional Gaussian component. Below 1 keV, the non-variable behaviour of the distant scattering off the NLR can be witnessed in the top panels of Fig. 7 or in the first bin of the excess variance spectra in both Figs 6 and 8.

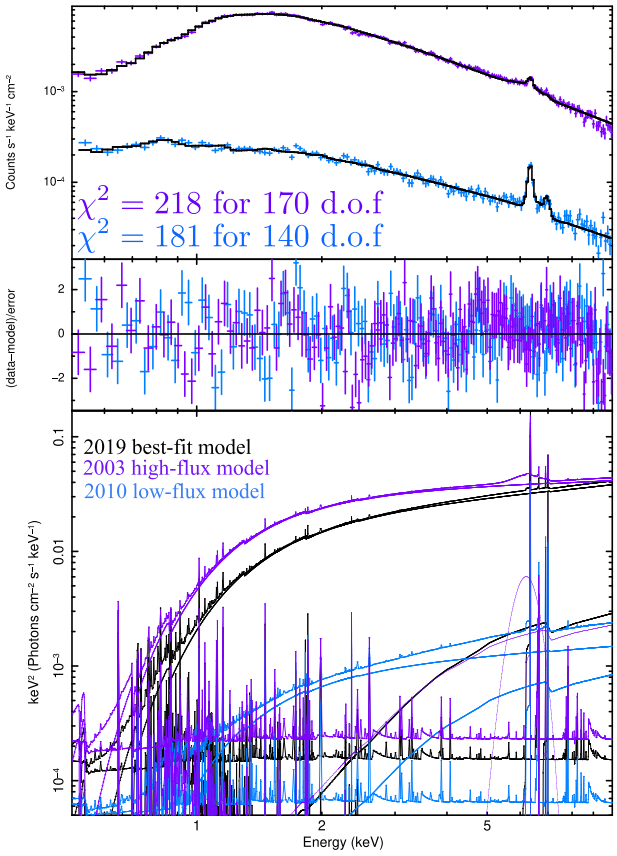

Figure 15. Fit to the high (purple) and low (dodger blue) flux states data using model 1 presented in Section 4.3 and based on the 2019 *XMM–Newton/NuSTAR* exposures.

In conclusion, the X-ray emission of NGC 2992 is due to a remarkably variable power-law-like continuum, possibly associated with a very hot corona, that is absorbed and reflected by gas whose $N_{\mathrm{H}} < 1.5 \times 10^{24}$ cm^{-2} (globally Compton-thin). The strong amplitude variations coupled with the very weak spectral changes are somehow suggesting the hot corona in NGC 2992 to be rather peculiar, and additional efforts must be made to clarify the physical properties of this medium.

ACKNOWLEDGEMENTS

We thank the referee for her/his useful comments. Part of this work is based on archival data, software or online services provided by the Space Science Data Center - ASI. 'This work has been partially

[4]This exposure, taken in full frame observing mode, is severely affected by pile-up. To mitigate this issue, we used an annular region to extract the source spectrum with r_{in} and r_{out} being 10 arcsec and 40 arcsec, respectively.

supported by the ASI-INAF program I/004/11/4. RM acknowledges financial contribution from the agreement ASI-INAF n.2017-14-H.0. SB acknowledges financial support from ASI under grants ASI-INAF I/037/12/0 and n. 2017-14-H.O. BDM acknowledges support via Ramón y Cajal Fellowship RYC2018-025950-I. AL acknowledges support from the HORIZON-2020 grant 'Integrated Activities for the High Energy Astrophysics Domain' (AHEAD-2020), G.A. 871158. This work is based on observations obtained with: the NuSTAR mission, a project led by the California Institute of Technology, managed by the Jet Propulsion Laboratory and funded by NASA; *XMM–Newton*, an ESA science mission with instruments and contributions directly funded by ESA Member States and the USA (NASA).

DATA AVAILABILITY

The *XMM–Newton* data can be downloaded directly from the mission archive at the web page https://www.cosmos.esa.int/web/xmm-newton/xsa, while *NuSTAR* and *Swift* exposures can be easily downloaded using the *BROWSE* tool at the web pages https://heasarc.gsfc.nasa.gov/cgi-bin/W3Browse/w3browse.pl or from the official mirror archives hosted by the Space Science Data Center of the Italian Space Agency https://www.ssdc.asi.it/mma.html.

REFERENCES

Almaini O. et al., 2000, MNRAS, 315, 325
Alston W. N. et al., 2019, MNRAS, 482, 2088
Arnaud K. A., 1996, ASP Conf. Ser. Vol. 101, XSPEC: The First Ten Years. Astron. Soc. Pac., San Francisco, p. 17
Awaki H., Koyama K., Inoue H., Halpern J. P., 1991, PASJ, 43, 195
Awaki H., Ueno S., Taniguchi Y., Weaver K. A., 2000, ApJ, 542, 175
Baloković M. et al., 2018, ApJ, 854, 42
Baloković M., García J. A., Cabral S. E., 2019, Res. Notes Am. Astron. Soc., 3, 173
Baloković M., Cabral S. E., Brenneman L., Urry C. M., 2021, ApJ, 916, 90
Barr P., Mushotzky R. F., 1986, Nature, 320, 421
Bauer A., Baltay C., Coppi P., Ellman N., Jerke J., Rabinowitz D., Scalzo R., 2009, ApJ, 696, 1241
Beloborodov A. M., 1999, in Poutanen J., Svensson R., eds, ASP Conf. Ser. Vol. 161, High Energy Processes in Accreting Black Holes. Astron. Soc. Pac., San Francisco, p. 295
Bianchi S., Guainazzi M., Chiaberge M., 2006, A&A, 448, 499
Bianchi S., Guainazzi M., Matt G., Fonseca Bonilla N., Ponti G., 2009, A&A, 495, 421
Bianchi S., Chiaberge M., Evans D. A., Guainazzi M., Baldi R. D., Matt G., Piconcelli E., 2010, MNRAS, 405, 553
Brenneman L. W., Reynolds C. S., 2009, ApJ, 702, 1367
Cappi M. et al., 1999, A&A, 344, 857
Cash W., 1979, ApJ, 228, 939
Colbert E. J. M., Strickland D. K., Veilleux S., Weaver K. A., 2005, ApJ, 628, 113
Dadina M., 2007, A&A, 461, 1209
de Gouveia Dal Pino E. M., Piovezan P. P., Kadowaki L. H. S., 2010, A&A, 518, A5
De Marco B. et al., 2020, A&A, 634, A65
de Vries W. H., Becker R. H., White R. L., Loomis C., 2005, AJ, 129, 615
di Clemente A., Giallongo E., Natali G., Trevese D., Vagnetti F., 1996, ApJ, 463, 466
Edelson R., Turner T. J., Pounds K., Vaughan S., Markowitz A., Marshall H., Dobbie P., Warwick R., 2002, ApJ, 568, 610
Edelson R. et al., 2015, ApJ, 806, 129
Fabian A. C., Nandra K., Reynolds C. S., Brandt W. N., Otani C., Tanaka Y., Inoue H., Iwasawa K., 1995, MNRAS, 277, L11
Fabian A. C., Lohfink A., Kara E., Parker M. L., Vasudevan R., Reynolds C. S., 2015, MNRAS, 451, 4375
Fabian A. C., Lohfink A., Belmont R., Malzac J., Coppi P., 2017, MNRAS, 467, 2566
Falocco S. et al., 2017, A&A, 608, A32
Ferland G. J. et al., 2017, Rev. Mex. Astron. Astrofis., 53, 385
Fernandez L. C., Secrest N. J., Johnson M. C., Schmitt H. R., Fischer T. C., Cigan P. J., Dorland B. N., 2022, ApJ, 927, 18
Gallo L. C., Blue D. M., Grupe D., Komossa S., Wilkins D. R., 2018, MNRAS, 478, 2557
Ghosh R., Pal M., 2021, Res. Notes Am. Astron. Soc., 5, 35
Green A. R., McHardy I. M., Lehto H. J., 1993, MNRAS, 265, 664
Guainazzi M., Bianchi S., 2007, MNRAS, 374, 1290
Guolo M., Ruschel-Dutra D., Grupe D., Peterson B. M., Storchi-Bergmann T., Schimoia J., Nemmen R., Robinson A., 2021, MNRAS, 508, 144
Haardt F., Maraschi L., 1991, ApJ, 380, L51
Haardt F., Maraschi L., 1993, ApJ, 413, 507
Harrison F. A. et al., 2013, ApJ, 770, 103
Igo Z. et al., 2020, MNRAS, 493, 1088
Keel W. C., 1996, ApJS, 106, 27
Laha S., Ghosh R., 2021, ApJ, 915, 93
Laha S., Markowitz A. G., Krumpe M., Nikutta R., Rothschild R., Saha T., 2020, ApJ, 897, 66
Laha S. et al., 2022, preprint (arXiv:2203.07446)
Laurenti M., Vagnetti F., Middei R., Paolillo M., 2020, MNRAS, 499, 6053
Lawrence A., Papadakis I., 1993, ApJ, 414, L85
Lusso E., Risaliti G., 2017, A&A, 602, A79
Lusso E. et al., 2010, A&A, 512, A34
Madejski G. M. et al., 1995, ApJ, 438, 672
Malizia A., Molina M., Bassani L., Stephen J. B., Bazzano A., Ubertini P., Bird A. J., 2014, ApJ, 782, L25
Marinucci A., Bianchi S., Matt G., Fabian A. C., Iwasawa K., Miniutti G., Piconcelli E., 2011, A&A, 526, A36
Marinucci A., Bianchi S., Fabbiano G., Matt G., Risaliti G., Nardini E., Wang J., 2017, MNRAS, 470, 4039
Marinucci A., Bianchi S., Braito V., Matt G., Nardini E., Reeves J., 2018, MNRAS, 478, 5638
Marinucci A., Bianchi S., Braito V., De Marco B., Matt G., Middei R., Nardini E., Reeves J. N., 2020, MNRAS, 496, 3412
Matt G., 2002, Phil. Trans. R. Soc. Lond. Ser. A, 360, 2045
Matt G., Fabian A. C., Ross R. R., 1993, MNRAS, 262, 179
Matt G. et al., 2015, MNRAS, 447, 3029
Matzeu G. A., Reeves J. N., Nardini E., Braito V., Costa M. T., Tombesi F., Gofford J., 2016, MNRAS, 458, 1311
Matzeu G. A., Reeves J. N., Nardini E., Braito V., Turner T. J., Costa M. T., 2017, MNRAS, 465, 2804
McHardy I. M., Koerding E., Knigge C., Uttley P., Fender R. P., 2006, Nature, 444, 730
Mehdipour M., Kaastra J. S., Kallman T., 2016, A&A, 596, A65
Middei R., Vagnetti F., Bianchi S., La Franca F., Paolillo M., Ursini F., 2017, A&A, 599, A82
Middei R., Bianchi S., Marinucci A., Matt G., Petrucci P. O., Tamborra F., Tortosa A., 2019, A&A, 630, A131
Middei R. et al., 2021, A&A, 647, A102
Miller J. M. et al., 2015, Nature, 526, 542
Molendi S., Bianchi S., Matt G., 2003, MNRAS, 343, L1
Molina M. et al., 2009, MNRAS, 399, 1293
Molina M., Bassani L., Malizia A., Stephen J. B., Bird A. J., Bazzano A., Ubertini P., 2013, MNRAS, 433, 1687
Murphy K. D., Yaqoob T., 2009, MNRAS, 397, 1549
Nandra K., 2001, Adv. Space Res., 28, 295
Nandra K., George I. M., Mushotzky R. F., Turner T. J., Yaqoob T., 1997, ApJ, 476, 70
O'Neill P. M., Nandra K., Papadakis I. E., Turner T. J., 2005, MNRAS, 358, 1405
Padovani P. et al., 2017, A&AR, 25, 2
Paolillo M. et al., 2017, MNRAS, 471, 4398
Papadakis I. E., 2004, MNRAS, 348, 207

Papadakis I. E., Chatzopoulos E., Athanasiadis D., Markowitz A., Georgantopoulos I., 2008, A&A, 487, 475
Parker M. L., Alston W. N., Igo Z., Fabian A. C., 2020, MNRAS, 492, 1363
Perola G. C., Matt G., Cappi M., Fiore F., Guainazzi M., Maraschi L., Petrucci P. O., Piro L., 2002, A&A, 389, 802
Ponti G., Cappi M., Dadina M., Malaguti G., 2004, A&A, 417, 451
Ponti G., Miniutti G., Cappi M., Maraschi L., Fabian A. C., Iwasawa K., 2006, MNRAS, 368, 903
Ponti G., Papadakis I., Bianchi S., Guainazzi M., Matt G., Uttley P., Bonilla N. F., 2012, A&A, 542, A83
Porquet D. et al., 2018, A&A, 609, A42
Poutanen J., Fabian A. C., 1999, MNRAS, 306, L31
Ricci C. et al., 2018, MNRAS, 480, 1819
Ricci C. et al., 2020, ApJ, 898, L1
Ricci C. et al., 2021, ApJS, 255, 7
Rybicki G. B., Lightman A. P., 1979, Radiative Processes in Astrophysics. John Wiley & Sons, Inc.
Schlafly E. F., Finkbeiner D. P., 2011, ApJ, 737, 103
Serafinelli R., Vagnetti F., Middei R., 2017, A&A, 600, A101
Shu X. W., Yaqoob T., Murphy K. D., Braito V., Wang J. X., Zheng W., 2010, ApJ, 713, 1256
Simonetti J. H., Cordes J. M., Heeschen D. S., 1985, ApJ, 296, 46
Sobolewska M. A., Papadakis I. E., 2009, MNRAS, 399, 1597
Sunyaev R. A., Titarchuk L. G., 1980, A&A, 500, 167
Tortosa A. et al., 2018, MNRAS, 473, 3104
Trevese D., Kron R. G., Majewski S. R., Bershady M. A., Koo D. C., 1994, ApJ, 433, 494
Trippe M. L., Crenshaw D. M., Deo R., Dietrich M., 2008, AJ, 135, 2048
Turner T. J., George I. M., Nandra K., Mushotzky R. F., 1997a, ApJS, 113, 23
Turner T. J., George I. M., Nandra K., Mushotzky R. F., 1997b, ApJ, 488, 164
Uttley P., McHardy I. M., Papadakis I. E., 2002, MNRAS, 332, 231
Uttley P., McHardy I. M., Vaughan S., 2005, MNRAS, 359, 345
Vagnetti F., Turriziani S., Trevese D., 2011, A&A, 536, A84
Vagnetti F., Middei R., Antonucci M., Paolillo M., Serafinelli R., 2016, A&A, 593, A55
Vaughan S., Edelson R., Warwick R. S., Uttley P., 2003, MNRAS, 345, 1271
Vaughan S., Fabian A. C., Ballantyne D. R., De Rosa A., Piro L., Matt G., 2004, MNRAS, 351, 193
Yaqoob T., 2012, MNRAS, 423, 3360
Yaqoob T. et al., 2007, PASJ, 59, 283
Zdziarski A. A., Johnson W. N., Done C., Smith D., McNaron-Brown K., 1995, ApJ, 438, L63
Zdziarski A. A., Johnson W. N., Magdziarz P., 1996, MNRAS, 283, 193
Życki P. T., Done C., Smith A. D., 1999, MNRAS, 309, 561

APPENDIX A: SOME EXTRA MATERIAL

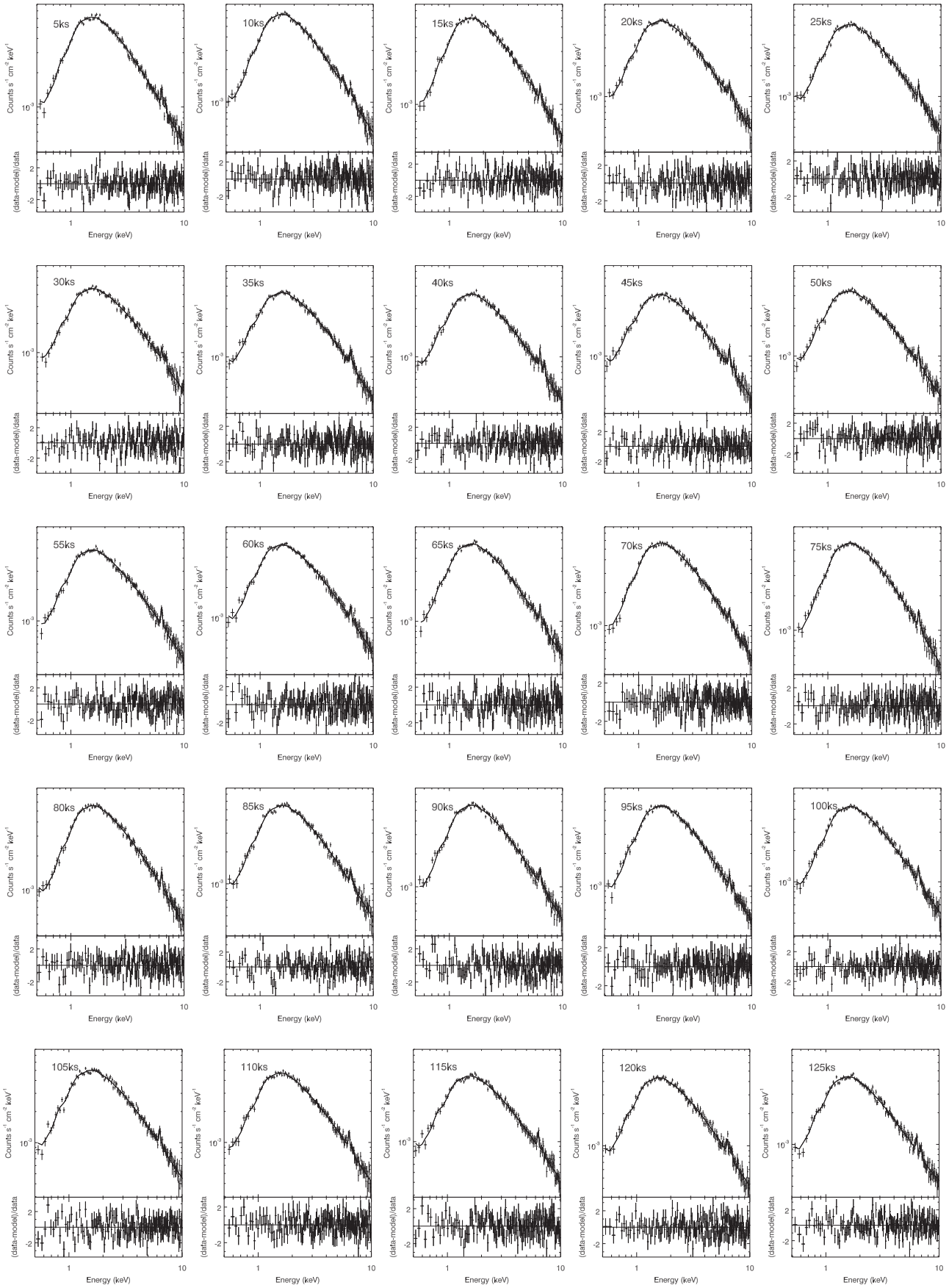

Figure A1. Spectral slices ∼5 ks long best fitted in accordance with Section 5.4.

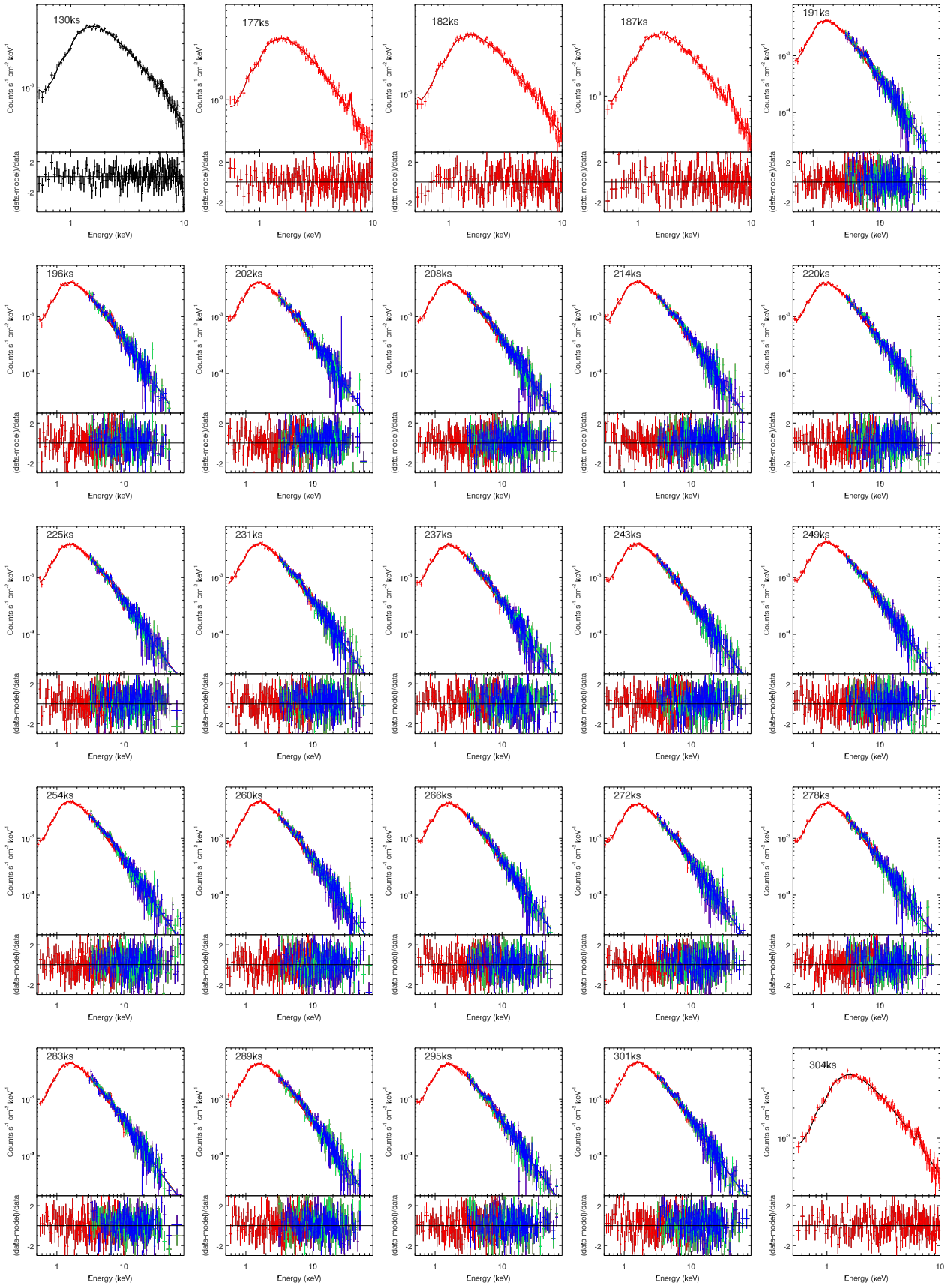

Figure A2. Continues Fig. A1.

Table A1. Best-fitting parameters derived form the analysis of XRT exposures. Fluxes in the 0.5–2 and 2–10 keV are reported in units of $\times 10^{-12}$ and $\times 10^{-11}$ erg cm^{-2} s^{-1}, respectively. The column density accounts for 10^{22} cm^{-2} and normalizations are listed in units of photons keV^{-1} cm^{-2} s^{-1}.

Date	Obs. ID.	$F_{0.5-2\,\mathrm{keV}}$	$F_{2-10\,\mathrm{keV}}$	N_{H}	Γ	Norm
2006-06-14	00035344002	1.16 ± 0.23	2.30 ± 0.23	0.23 ± 0.22	0.90 ± 0.20	0.0008 ± 0.0002
2006-06-25	00035344003	0.68 ± 0.09	0.98 ± 0.09	0.19 ± 0.14	1.05 ± 0.17	0.0005 ± 0.0001
2006-07-06	00035344004	0.67 ± 0.09	0.97 ± 0.09	0.16 ± 0.13	0.90 ± 0.14	0.0004 ± 0.0001
2006-07-07	00035344005	0.85 ± 0.06	0.59 ± 0.06	0.22 ± 0.07	1.16 ± 0.08	0.0006 ± 0.0001
2006-07-11	00035344006	0.78 ± 0.16	1.37 ± 0.16	0.18 ± 0.16	1.19 ± 0.24	0.0005 ± 0.0002
2006-07-12	00035344007	0.80 ± 0.21	1.63 ± 0.21	0.34 ± 0.28	1.29 ± 0.28	0.0007 ± 0.0003
2015-12-02	00081055001	6.60 ± 0.27	3.14 ± 0.27	0.89 ± 0.10	1.52 ± 0.06	0.0123 ± 0.0011
2017-06-02	00035344008	4.19 ± 0.29	2.86 ± 0.29	0.58 ± 0.12	1.31 ± 0.09	0.0052 ± 0.0006
2017-06-04	00035344009	4.65 ± 0.45	4.77 ± 0.45	0.80 ± 0.22	1.45 ± 0.13	0.0077 ± 0.0015
2019-03-26	00035344010	11.80 ± 0.71	6.87 ± 0.71	0.81 ± 0.13	1.63 ± 0.09	0.0211 ± 0.0026
2019-03-30	00035344011	14.24 ± 0.91	7.82 ± 0.91	0.79 ± 0.14	1.70 ± 0.09	0.0258 ± 0.0033
2019-04-03	00035344012	8.72 ± 0.62	6.18 ± 0.62	0.84 ± 0.18	1.54 ± 0.11	0.0155 ± 0.0024
2019-04-07	00035344013	10.01 ± 0.83	7.48 ± 0.83	0.79 ± 0.19	1.57 ± 0.12	0.017 ± 0.003
2019-04-11	00035344014	6.33 ± 0.58	5.32 ± 0.58	0.44 ± 0.15	1.24 ± 0.11	0.0064 ± 0.0010
2019-04-14	00035344015	10.83 ± 0.77	7.95 ± 0.77	0.74 ± 0.15	1.56 ± 0.10	0.0174 ± 0.0025
2019-04-19	00035344016	7.75 ± 0.55	6.03 ± 0.55	0.57 ± 0.14	1.29 ± 0.10	0.0094 ± 0.0013
2019-04-23	00035344017	8.78 ± 0.60	6.32 ± 0.60	0.63 ± 0.13	1.39 ± 0.10	0.0118 ± 0.0016
2019-05-01	00035344019	10.21 ± 0.82	7.67 ± 0.82	0.90 ± 0.17	1.61 ± 0.11	0.0198 ± 0.0031
2019-05-04	00035344020	7.28 ± 0.63	6.76 ± 0.63	0.75 ± 0.20	1.42 ± 0.13	0.0113 ± 0.002
2019-05-06	00035344021	9.73 ± 0.68	6.24 ± 0.68	0.81 ± 0.15	1.58 ± 0.1	0.0171 ± 0.0024
2019-05-08	00035344022	9.55 ± 0.62	6.47 ± 0.62	0.81 ± 0.15	1.48 ± 0.09	0.0161 ± 0.0021
2019-05-10	00035344023	9.46 ± 1.33	11.36 ± 1.33	0.70 ± 0.24	1.50 ± 0.17	0.0143 ± 0.0034
2019-05-12	00035344024	11.91 ± 5.47	9.60 ± 1.47	0.76 ± 0.57	1.53 ± 0.39	0.0194 ± 0.0109
2019-05-14	00035344025	12.80 ± 0.68	7.36 ± 0.68	0.80 ± 0.13	1.57 ± 0.08	0.0221 ± 0.0026
2019-05-16	00035344026	15.48 ± 0.92	6.97 ± 0.92	0.85 ± 0.13	1.74 ± 0.09	0.0302 ± 0.0036
2019-05-18	00035344027	10.39 ± 0.68	6.92 ± 0.68	0.82 ± 0.15	1.54 ± 0.10	0.0181 ± 0.0025
2019-05-20	00035344028	11.53 ± 0.71	6.33 ± 0.71	0.93 ± 0.15	1.69 ± 0.09	0.0238 ± 0.0031
2019-05-22	00035344029	12.44 ± 0.74	7.10 ± 0.74	0.88 ± 0.15	1.67 ± 0.10	0.0243 ± 0.0032
2019-05-24	00035344030	11.33 ± 0.74	6.80 ± 0.74	0.57 ± 0.11	1.47 ± 0.09	0.0145 ± 0.0017
2019-05-26	00035344031	10.34 ± 0.68	6.20 ± 0.68	0.66 ± 0.12	1.51 ± 0.09	0.0151 ± 0.0019
2019-05-28	00035344032	8.42 ± 0.64	6.09 ± 0.64	0.87 ± 0.18	1.54 ± 0.11	0.0155 ± 0.0023
2019-05-30	00035344033	9.43 ± 0.67	6.56 ± 0.67	0.87 ± 0.17	1.56 ± 0.11	0.0175 ± 0.0026
2019-06-01	00035344034	10.19 ± 0.74	7.04 ± 0.74	0.62 ± 0.15	1.46 ± 0.10	0.0138 ± 0.002
2019-06-03	00035344035	7.67 ± 0.59	6.19 ± 0.59	0.52 ± 0.13	1.26 ± 0.10	0.0086 ± 0.0012
2019-06-05	00035344036	15.33 ± 0.92	8.89 ± 0.92	0.83 ± 0.15	1.64 ± 0.10	0.0282 ± 0.0037
2019-06-07	00035344037	8.15 ± 0.61	6.60 ± 0.61	0.62 ± 0.13	1.33 ± 0.09	0.0106 ± 0.0014
2019-06-09	00035344038	5.87 ± 0.49	5.00 ± 0.49	0.80 ± 0.20	1.53 ± 0.13	0.01 ± 0.0018
2019-06-11	00035344039	10.12 ± 0.66	6.27 ± 0.66	0.88 ± 0.14	1.59 ± 0.09	0.0192 ± 0.0025
2019-06-16	00035344040	7.40 ± 0.58	5.25 ± 0.58	0.60 ± 0.14	1.38 ± 0.10	0.0095 ± 0.0013
2019-06-20	00035344041	10.63 ± 0.66	6.17 ± 0.66	0.83 ± 0.14	1.61 ± 0.09	0.0192 ± 0.0025
2019-06-24	00035344042	6.99 ± 0.62	5.94 ± 0.62	0.74 ± 0.19	1.51 ± 0.13	0.011 ± 0.002
2019-06-27	00035344043	4.82 ± 1.37	5.29 ± 1.37	0.13 ± 0.23	0.62 ± 0.27	0.0026 ± 0.001
2019-10-09	00035344044	11.99 ± 0.80	7.50 ± 0.80	0.77 ± 0.13	1.57 ± 0.09	0.0201 ± 0.0025
2019-10-13	00035344045	4.22 ± 0.40	4.00 ± 0.40	0.39 ± 0.13	1.21 ± 0.11	0.004 ± 0.0006
2019-10-17	00035344046	5.57 ± 0.49	4.71 ± 0.49	0.68 ± 0.18	1.39 ± 0.12	0.0079 ± 0.0013
2019-10-21	00035344047	5.71 ± 0.67	6.88 ± 0.67	0.52 ± 0.22	1.31 ± 0.16	0.0065 ± 0.0015
2019-10-25	00035344048	6.21 ± 0.64	5.65 ± 0.64	0.80 ± 0.23	1.57 ± 0.15	0.0107 ± 0.0022
2019-10-29	00035344049	5.86 ± 0.55	6.52 ± 0.55	0.49 ± 0.20	1.14 ± 0.13	0.0061 ± 0.0012
2019-11-02	00035344050	4.05 ± 0.45	4.56 ± 0.45	0.43 ± 0.18	1.19 ± 0.14	0.004 ± 0.0008
2019-11-06	00035344051	4.57 ± 0.61	5.98 ± 0.61	0.64 ± 0.24	1.42 ± 0.17	0.0063 ± 0.0015
2019-11-08	00035344052	4.99 ± 0.42	3.87 ± 0.42	0.60 ± 0.15	1.43 ± 0.11	0.0066 ± 0.001
2019-11-10	00035344053	7.22 ± 0.61	5.93 ± 0.61	0.77 ± 0.17	1.47 ± 0.11	0.0115 ± 0.0018
2019-11-12	00035344054	7.29 ± 0.58	5.55 ± 0.58	0.88 ± 0.17	1.63 ± 0.11	0.0141 ± 0.0022
2019-11-14	00035344055	9.14 ± 0.71	7.40 ± 0.71	0.54 ± 0.13	1.27 ± 0.10	0.0106 ± 0.0014
2019-11-16	00035344056	7.68 ± 0.58	6.07 ± 0.58	0.82 ± 0.17	1.48 ± 0.11	0.013 ± 0.0019
2019-11-17	00035344057	10.62 ± 0.69	6.58 ± 0.69	0.85 ± 0.13	1.57 ± 0.09	0.0193 ± 0.0024
2019-11-20	00035344058	8.13 ± 0.65	6.70 ± 0.65	0.76 ± 0.17	1.41 ± 0.11	0.0126 ± 0.0019
2019-11-22	00035344059	7.80 ± 0.98	9.19 ± 0.98	0.52 ± 0.2	1.31 ± 0.15	0.0089 ± 0.0018
2019-11-26	00035344061	4.92 ± 0.49	4.27 ± 0.49	0.63 ± 0.18	1.42 ± 0.13	0.0067 ± 0.0012
2019-11-28	00035344062	10.67 ± 0.83	7.15 ± 0.83	0.66 ± 0.15	1.58 ± 0.11	0.0159 ± 0.0024
2019-11-30	00035344063	7.84 ± 0.73	6.63 ± 0.73	0.78 ± 0.18	1.53 ± 0.12	0.013 ± 0.0022
2019-12-02	00035344064	7.08 ± 0.63	4.54 ± 0.63	0.72 ± 0.17	1.77 ± 0.12	0.0122 ± 0.002

Table A1 – *continued*

Date	Obs. ID.	$F_{0.5–2\,\mathrm{keV}}$	$F_{2–10\,\mathrm{keV}}$	N_{H}	Γ	Norm
2019-12-04	00035344065	10.82 ± 0.75	7.92 ± 0.75	0.57 ± 0.12	1.37 ± 0.09	0.0135 ± 0.0017
2019-12-06	00035344066	14.79 ± 1.07	8.81 ± 1.07	0.83 ± 0.15	1.72 ± 0.10	0.028 ± 0.004
2019-12-08	00035344067	11.25 ± 0.78	7.60 ± 0.78	0.65 ± 0.15	1.47 ± 0.10	0.016 ± 0.0023
2019-12-10	00035344068	7.88 ± 1.00	8.39 ± 1.00	0.69 ± 0.26	1.54 ± 0.18	0.012 ± 0.0029
2019-12-12	00035344069	9.70 ± 0.67	6.20 ± 0.67	0.70 ± 0.13	1.55 ± 0.09	0.015 ± 0.0019
2019-12-14	00035344070	9.36 ± 0.74	6.57 ± 0.74	0.89 ± 0.19	1.66 ± 0.12	0.0185 ± 0.0031
2019-12-31	00035344071	2.96 ± 0.32	2.91 ± 0.32	0.53 ± 0.18	1.51 ± 0.15	0.0037 ± 0.0007
2020-01-28	00035344072	11.64 ± 0.97	8.21 ± 0.97	0.71 ± 0.15	1.63 ± 0.12	0.0187 ± 0.0029
2020-03-25	00035344073	12.08 ± 0.79	7.11 ± 0.79	0.74 ± 0.14	1.55 ± 0.09	0.0193 ± 0.0025
2020-05-19	00035344074	6.97 ± 0.58	5.79 ± 0.58	0.83 ± 0.19	1.58 ± 0.12	0.0125 ± 0.0021
2021-01-24	00035344075	3.31 ± 0.29	3.11 ± 0.29	0.49 ± 0.14	1.29 ± 0.11	0.0037 ± 0.0006
2021-01-29	00035344076	2.95 ± 0.41	3.98 ± 0.41	0.65 ± 0.25	1.41 ± 0.18	0.0041 ± 0.001
2021-02-03	00035344077	1.54 ± 0.84	9.94 ± 0.84	0.58 ± 0.68	1.11 ± 0.47	0.0017 ± 0.0012
2021-02-08	00035344078	1.60 ± 0.30	2.09 ± 0.30	0.83 ± 0.36	1.82 ± 0.26	0.0032 ± 0.0011
2021-02-13	00035344079	2.98 ± 0.32	3.07 ± 0.32	0.77 ± 0.23	1.52 ± 0.15	0.0049 ± 0.001
2021-02-18	00035344080	2.22 ± 0.42	3.81 ± 0.42	0.58 ± 0.33	1.34 ± 0.23	0.0028 ± 0.0009
2021-02-22	00035344081	5.27 ± 0.49	4.36 ± 0.49	0.84 ± 0.24	1.71 ± 0.15	0.0101 ± 0.0021
2021-02-28	00035344082	1.65 ± 0.22	2.27 ± 0.22	0.32 ± 0.17	1.17 ± 0.17	0.0014 ± 0.0003
2021-03-05	00035344083	1.50 ± 0.19	2.32 ± 0.19	0.28 ± 0.19	0.94 ± 0.16	0.0011 ± 0.0002
2021-03-10	00035344084	1.04 ± 0.19	1.46 ± 0.19	0.12 ± 0.14	1.14 ± 0.20	0.0006 ± 0.0002
2021-03-15	00035344085	1.37 ± 0.22	1.71 ± 0.22	0.42 ± 0.20	1.50 ± 0.20	0.0015 ± 0.0004
2021-03-25	00035344088	2.23 ± 0.25	2.78 ± 0.25	0.38 ± 0.16	1.18 ± 0.14	0.0021 ± 0.0004
2021-03-30	00035344089	2.00 ± 0.30	2.95 ± 0.30	0.35 ± 0.21	1.09 ± 0.17	0.0017 ± 0.0004
2021-04-04	00035344090	2.00 ± 0.26	2.19 ± 0.26	0.41 ± 0.17	1.40 ± 0.16	0.0021 ± 0.0004
2021-04-09	00035344091	3.14 ± 0.34	3.27 ± 0.34	0.84 ± 0.27	1.61 ± 0.17	0.0058 ± 0.0014
2021-04-14	00035344092	1.52 ± 0.22	1.65 ± 0.22	0.50 ± 0.22	1.58 ± 0.20	0.0019 ± 0.0005
2021-04-19	00035344093	2.31 ± 0.23	2.68 ± 0.23	0.28 ± 0.14	0.99 ± 0.13	0.0017 ± 0.0003
2021-04-24	00035344094	1.85 ± 0.27	2.57 ± 0.27	0.61 ± 0.25	1.36 ± 0.18	0.0024 ± 0.0006
2021-04-30	00035344096	2.76 ± 0.30	3.11 ± 0.30	0.62 ± 0.21	1.38 ± 0.15	0.0036 ± 0.0008
2021-05-04	00035344097	1.76 ± 0.23	2.70 ± 0.23	0.15 ± 0.12	0.93 ± 0.15	0.0011 ± 0.0002
2021-05-09	00035344098	1.01 ± 0.29	2.40 ± 0.29	0.43 ± 0.34	1.37 ± 0.32	0.0011 ± 0.0004
2021-05-12	00035344099	1.34 ± 0.26	2.47 ± 0.26	0.24 ± 0.20	1.08 ± 0.21	0.0010 ± 0.0003
2021-05-14	00035344100	2.08 ± 0.27	2.80 ± 0.27	0.46 ± 0.17	1.26 ± 0.15	0.0022 ± 0.0004
2021-05-19	00035344101	2.12 ± 0.29	2.85 ± 0.29	0.58 ± 0.28	1.38 ± 0.20	0.0027 ± 0.0007
2021-05-24	00035344102	2.32 ± 0.25	3.08 ± 0.25	0.40 ± 0.17	0.96 ± 0.13	0.0020 ± 0.0004
2021-05-29	00035344103	1.38 ± 0.30	3.46 ± 0.30	0.20 ± 0.16	0.82 ± 0.23	0.0008 ± 0.0002
2021-06-03	00035344104	0.90 ± 0.19	1.74 ± 0.19	0.30 ± 0.22	1.11 ± 0.21	0.0007 ± 0.0002
2021-06-08	00035344105	1.88 ± 0.41	3.37 ± 0.41	0.72 ± 0.39	1.68 ± 0.29	0.0031 ± 0.0012
2021-06-13	00035344106	2.27 ± 0.33	2.91 ± 0.33	0.70 ± 0.31	1.54 ± 0.21	0.0035 ± 0.001
2021-06-18	00035344107	1.47 ± 0.18	2.28 ± 0.18	0.25 ± 0.15	0.95 ± 0.15	0.0011 ± 0.0002
2021-06-23	00035344108	3.00 ± 0.28	2.78 ± 0.28	0.66 ± 0.19	1.42 ± 0.13	0.0042 ± 0.0008
2021-06-27	00035344109	2.43 ± 0.27	2.57 ± 0.27	0.51 ± 0.19	1.35 ± 0.15	0.0028 ± 0.0006
2021-07-03	00035344110	2.29 ± 0.36	3.52 ± 0.36	1.10 ± 0.36	1.70 ± 0.21	0.0056 ± 0.0017
2021-07-08	00035344111	2.60 ± 0.29	3.03 ± 0.29	0.46 ± 0.20	1.19 ± 0.15	0.0026 ± 0.0006
2021-07-13	00035344112	4.03 ± 0.39	3.66 ± 0.39	0.64 ± 0.19	1.46 ± 0.14	0.0056 ± 0.0011
2021-10-08	00035344113	3.58 ± 0.37	3.42 ± 0.37	0.55 ± 0.17	1.43 ± 0.13	0.0044 ± 0.0008
2021-10-13	00035344114	3.61 ± 0.30	3.21 ± 0.30	0.51 ± 0.13	1.27 ± 0.11	0.0040 ± 0.0006
2021-10-18	00035344115	3.55 ± 0.45	4.91 ± 0.45	0.80 ± 0.27	1.43 ± 0.17	0.0058 ± 0.0014
2021-10-19	00035344116	4.61 ± 0.85	8.54 ± 0.85	0.77 ± 0.38	1.43 ± 0.25	0.0073 ± 0.0025
2021-10-21	00035344117	2.99 ± 0.52	5.37 ± 0.52	0.70 ± 0.30	1.38 ± 0.22	0.0043 ± 0.0013
2021-10-23	00035344118	2.59 ± 0.37	3.20 ± 0.37	0.74 ± 0.26	1.55 ± 0.19	0.0041 ± 0.0011
2021-10-28	00035344119	4.01 ± 0.36	3.38 ± 0.36	0.65 ± 0.18	1.49 ± 0.13	0.0057 ± 0.001
2021-11-02	00035344120	5.66 ± 0.57	6.94 ± 0.57	0.66 ± 0.24	1.25 ± 0.15	0.0075 ± 0.0016
2021-11-07	00035344121	3.57 ± 0.32	3.31 ± 0.32	0.55 ± 0.17	1.31 ± 0.12	0.0042 ± 0.0007
2021-11-12	00035344122	5.43 ± 0.51	5.01 ± 0.51	0.62 ± 0.17	1.40 ± 0.13	0.0073 ± 0.0013
2021-11-17	00035344123	4.04 ± 0.44	3.65 ± 0.44	0.91 ± 0.25	1.71 ± 0.16	0.0083 ± 0.0018
2021-11-22	00035344124	6.69 ± 0.62	6.20 ± 0.62	0.62 ± 0.18	1.31 ± 0.12	0.0085 ± 0.0015
2021-12-02	00035344125	6.71 ± 0.61	6.75 ± 0.61	0.42 ± 0.14	1.20 ± 0.12	0.0065 ± 0.001
2021-12-12	00035344126	6.67 ± 0.76	7.98 ± 0.76	0.55 ± 0.20	1.26 ± 0.14	0.0078 ± 0.0015
2021-12-24	00035344128	3.50 ± 0.35	3.85 ± 0.35	0.35 ± 0.15	1.10 ± 0.12	0.0030 ± 0.0005
2021-12-28	00035344129	4.30 ± 0.30	3.90 ± 0.30	0.65 ± 0.20	1.35 ± 0.20	0.0057 ± 0.0003

Table A2. Best-fitting parameters of the time-resolved *XMM–Newton–NuSTAR* analysis. For each spectral slice, the corresponding ks are quoted. Fluxes are in units of erg cm^{-2} s^{-1} $\times$ 10^{-11} while Gaussian normalization accounts for 10^{-5} ph. cm^{-2} s^{-1}. The quoted normalization for power law and *MyTorus* are in units of ph. keV^{-1} cm^{-2} s^{-1}. Finally, $N_{\rm H}$ and $N_{\rm H}^{\rm MyT}$ are in units of 10^{22} and 10^{24} cm^{-2}, respectively.

Slice	$F_{0.3-2\,\rm keV}$	$F_{2-10\,\rm keV}$	$N_{\rm H}$	Γ	Norm$_{\rm po}$	$N_{\rm H}^{\rm MyT}$	Norm$^{\rm MyT}$	Fe$_{\rm He\,\alpha}$	Fe$_{\rm Ly\,\alpha}$	Red flare	χ^2	d.o.f
5	1.51 ± 0.03	9.59 ± 0.42	0.77 ± 0.02	1.76 ± 0.03	0.025 ± 0.001	<0.77	0.26 ± 0.31	<2.62	3.22 ± 2.16	<3.3	160	153
10	1.57 ± 0.03	10.19 ± 0.25	0.78 ± 0.02	1.74 ± 0.03	0.027 ± 0.001	<0.78	0.13 ± 0.23	<3.78	<4.13	6.43 ± 2.9	164	156
15	1.47 ± 0.02	9.88 ± 0.26	0.77 ± 0.02	1.71 ± 0.03	0.025 ± 0.001	0.77 ± 0.06	0.120 ± 0.11	<3.38	<1.44	<5.0	167	154
20	1.35 ± 0.03	9.14 ± 0.41	0.77 ± 0.02	1.69 ± 0.04	0.022 ± 0.001	<0.77	0.24 ± 0.13	2.96 ± 2.05	<4.12	<1.26	164	152
25	1.24 ± 0.01	8.47 ± 0.26	0.78 ± 0.02	1.70 ± 0.03	0.021 ± 0.001	0.78 ± 0.17	0.07 ± 0.24	<2.62	<3.89	<3.03	136	155
30	1.13 ± 0.01	7.69 ± 0.22	0.79 ± 0.02	1.70 ± 0.03	0.019 ± 0.001	0.79 ± 0.17	0.05 ± 0.06	2.76 ± 1.91	3.35 ± 1.97	<3.39	210	151
35	1.07 ± 0.02	7.48 ± 0.26	0.75 ± 0.02	1.66 ± 0.04	0.017 ± 0.001	<0.75	0.10 ± 0.23	2.57 ± 1.89	<2.04	<1.93	132	150
40	1.03 ± 0.01	7.01 ± 0.22	0.78 ± 0.03	1.71 ± 0.03	0.017 ± 0.001	<0.78	0.08 ± 0.24	<2.62	4.01 ± 1.96	<1.24	143	150
45	1.02 ± 0.02	7.13 ± 0.33	0.74 ± 0.02	1.65 ± 0.04	0.016 ± 0.001	<0.74	0.22 ± 0.26	<2.14	2.32 ± 1.89	<0.88	169	151
50	1.10 ± 0.02	7.45 ± 0.61	0.75 ± 0.02	1.64 ± 0.04	0.016 ± 0.001	<0.75	0.33 ± 0.17	<1.66	<1.05	<2.42	163	151
55	1.18 ± 0.01	8.13 ± 0.26	0.76 ± 0.02	1.68 ± 0.03	0.019 ± 0.001	0.76 ± 0.13	0.07 ± 0.05	<1.72	<2.39	<1.85	173	151
60	1.30 ± 0.02	8.75 ± 0.55	0.76 ± 0.03	1.68 ± 0.03	0.021 ± 0.001	<0.76	0.3 ± 0.23	<2.62	2.75 ± 2.05	<3.86	155	154
65	1.34 ± 0.03	9.13 ± 0.38	0.79 ± 0.02	1.70 ± 0.03	0.022 ± 0.001	<0.79	0.2 ± 0.26	<1.86	<4.03	<4.56	179	154
70	1.39 ± 0.01	9.73 ± 0.23	0.78 ± 0.02	1.66 ± 0.03	0.023 ± 0.001	0.78 ± 0.75	0.05 ± 0.09	<1.63	<3.23	<2.2	123	153
75	1.40 ± 0.02	9.62 ± 0.32	0.79 ± 0.02	1.71 ± 0.03	0.024 ± 0.001	<0.79	0.15 ± 0.27	2.13 ± 2.08	<2.17	<2.54	152	151
80	1.36 ± 0.01	9.47 ± 0.30	0.78 ± 0.02	1.69 ± 0.03	0.023 ± 0.001	0.78 ± 0.27	0.05 ± 0.07	<1.95	<2.15	<3.86	158	155
85	1.34 ± 0.01	9.15 ± 0.48	0.78 ± 0.02	1.70 ± 0.03	0.022 ± 0.001	<0.78	0.03 ± 0.01	<3.98	<2.07	<1.8	200	154
90	1.36 ± 0.02	9.43 ± 0.61	0.80 ± 0.03	1.67 ± 0.02	0.022 ± 0.001	<0.8	0.54 ± 0.17	2.33 ± 2.02	<3.08	<1.3	181	153
95	1.33 ± 0.03	9.12 ± 0.47	0.79 ± 0.02	1.68 ± 0.03	0.022 ± 0.001	<0.79	0.21 ± 0.19	<2.29	<3.94	<2.94	130	152
100	1.29 ± 0.02	8.99 ± 0.27	0.78 ± 0.02	1.69 ± 0.03	0.022 ± 0.001	0.78 ± 0.06	0.1 ± 0.11	<3.94	<1.06	2.78 ± 2.64	161	155
105	1.23 ± 0.02	8.67 ± 0.30	0.77 ± 0.02	1.67 ± 0.04	0.020 ± 0.001	0.77 ± 0.12	0.1 ± 0.21	<3.88	<1.66	<1.77	189	154
110	1.15 ± 0.01	7.98 ± 0.30	0.80 ± 0.02	1.71 ± 0.03	0.020 ± 0.001	0.80 ± 0.38	0.06 ± 0.08	<3.63	<2.6	<3.22	133	152
115	1.09 ± 0.03	7.86 ± 0.43	0.75 ± 0.03	1.62 ± 0.04	0.016 ± 0.001	<0.75	0.21 ± 0.24	<2.25	<3.68	<1.79	161	152
120	1.07 ± 0.02	7.72 ± 0.23	0.76 ± 0.03	1.63 ± 0.04	0.017 ± 0.001	<0.76	0.12 ± 0.21	3.48 ± 1.94	3.29 ± 1.97	<0.77	158	151
125	1.08 ± 0.01	7.76 ± 0.46	0.75 ± 0.02	1.62 ± 0.03	0.017 ± 0.001	<0.75	0.02 ± 0.01	<1.99	3.36 ± 2.01	<3.08	178	151
130	1.14 ± 0.02	8.01 ± 0.24	0.79 ± 0.02	1.67 ± 0.03	0.019 ± 0.001	0.79 ± 0.13	0.06 ± 0.14	<3.27	2.61 ± 1.99	<4.24	162	152
177	0.95 ± 0.02	6.78 ± 0.32	0.76 ± 0.02	1.64 ± 0.03	0.015 ± 0.001	0.76 ± 0.04	0.17 ± 0.16	<1.2	<4.7	<2.12	135	147
182	0.99 ± 0.02	7.07 ± 0.21	0.73 ± 0.01	1.60 ± 0.02	0.015 ± 0.001	0.73 ± 0.03	0.07 ± 0.05	1.55 ± 1.12	<1.68	<1.75	165	151
187	1.02 ± 0.01	7.39 ± 0.30	0.75 ± 0.02	1.65 ± 0.02	0.016 ± 0.001	0.75 ± 0.04	0.12 ± 0.05	3.65 ± 1.18	2.01 ± 1.19	<2.05	189	151
191	1.03 ± 0.01	7.29 ± 0.25	0.78 ± 0.02	1.68 ± 0.02	0.017 ± 0.001	0.78 ± 0.04	0.09 ± 0.05	2.38 ± 1.63	2.14 ± 1.62	<3.92	447	393
196	0.99 ± 0.01	7.15 ± 0.28	0.79 ± 0.02	1.68 ± 0.02	0.016 ± 0.001	0.79 ± 0.04	0.09 ± 0.05	2.49 ± 1.61	<2.77	<2.25	424	390
202	0.99 ± 0.01	7.02 ± 0.25	0.79 ± 0.02	1.68 ± 0.02	0.016 ± 0.001	0.79 ± 0.04	0.08 ± 0.04	<1.48	<2.8	<1.54	469	401
208	1.00 ± 0.01	7.16 ± 0.25	0.80 ± 0.02	1.69 ± 0.02	0.017 ± 0.001	0.80 ± 0.04	0.08 ± 0.04	<1.02	<3.61	1.97 ± 1.76	440	420
214	1.01 ± 0.01	7.16 ± 0.26	0.78 ± 0.02	1.68 ± 0.02	0.017 ± 0.001	0.78 ± 0.04	0.09 ± 0.06	<2.37	2.26 ± 1.53	<1.09	447	429
220	0.97 ± 0.01	6.99 ± 0.28	0.77 ± 0.02	1.67 ± 0.02	0.016 ± 0.001	0.77 ± 0.04	0.10 ± 0.05	2.37 ± 1.58	<3.91	3.93 ± 1.98	438	415
225	0.97 ± 0.01	6.92 ± 0.27	0.78 ± 0.02	1.67 ± 0.02	0.016 ± 0.001	0.78 ± 0.03	0.09 ± 0.05	<2.09	1.6 ± 1.23	2.96 ± 1.93	430	420
231	0.97 ± 0.01	7.06 ± 0.25	0.81 ± 0.02	1.67 ± 0.02	0.016 ± 0.001	0.81 ± 0.07	0.07 ± 0.06	2.07 ± 1.54	<2.67	<3.12	456	427
237	0.93 ± 0.01	6.74 ± 0.27	0.81 ± 0.02	1.69 ± 0.02	0.015 ± 0.001	0.81 ± 0.03	0.13 ± 0.07	2.03 ± 1.5	<2.52	<2.53	485	426
243	0.97 ± 0.01	6.85 ± 0.28	0.77 ± 0.02	1.67 ± 0.02	0.016 ± 0.001	0.77 ± 0.04	0.10 ± 0.07	1.6 ± 1.48	<2.62	<2.92	490	428
249	1.04 ± 0.01	7.50 ± 0.26	0.78 ± 0.02	1.66 ± 0.02	0.017 ± 0.001	0.78 ± 0.06	0.07 ± 0.08	1.73 ± 1.62	<3.14	<2.43	433	430
254	1.10 ± 0.01	7.67 ± 0.27	0.79 ± 0.02	1.70 ± 0.02	0.018 ± 0.001	0.79 ± 0.04	0.10 ± 0.05	<2.03	1.88 ± 1.58	<2.72	438	426
260	1.08 ± 0.01	7.81 ± 0.29	0.82 ± 0.02	1.71 ± 0.02	0.019 ± 0.001	0.82 ± 0.04	0.10 ± 0.06	<3.1	<2.42 ± 1.65	<4.1	482	435
266	1.03 ± 0.01	7.42 ± 0.28	0.81 ± 0.02	1.68 ± 0.02	0.017 ± 0.001	0.81 ± 0.04	0.10 ± 0.07	<2.9	<2.02	2.62 ± 2.05	427	404
272	0.99 ± 0.01	7.23 ± 0.31	0.78 ± 0.02	1.67 ± 0.02	0.016 ± 0.001	0.78 ± 0.04	0.11 ± 0.06	<2.32	4.18 ± 1.66	3.38 ± 2.03	401	414
278	1.02 ± 0.01	7.54 ± 0.28	0.77 ± 0.02	1.64 ± 0.02	0.016 ± 0.001	0.77 ± 0.04	0.09 ± 0.06	<1.11	<2.81	3.14 ± 2.08	410	403
283	1.06 ± 0.01	7.59 ± 0.29	0.80 ± 0.02	1.69 ± 0.02	0.018 ± 0.001	0.80 ± 0.03	0.12 ± 0.07	<1.17	<1.65	<1.76	391	397
289	1.05 ± 0.01	7.63 ± 0.28	0.79 ± 0.02	1.67 ± 0.02	0.017 ± 0.001	0.79 ± 0.04	0.14 ± 0.1	<2.86	2.25 ± 1.61	<3.89	439	413
295	1.04 ± 0.01	7.48 ± 0.26	0.78 ± 0.02	1.66 ± 0.02	0.017 ± 0.001	0.78 ± 0.03	0.13 ± 0.08	<2.82	2.48 ± 1.59	2.14 ± 2.01	480	423
301	1.09 ± 0.01	7.89 ± 0.26	0.80 ± 0.02	1.68 ± 0.02	0.018 ± 0.001	0.80 ± 0.03	0.10 ± 0.05	1.77 ± 1.62	1.74 ± 1.61	<2.29	501	439
304	1.06 ± 0.03	8.0 ± 0.5	0.77 ± 0.03	1.62 ± 0.05	0.017 ± 0.001	<0.77	0.22 ± 0.2	3.77 ± 2.53	<3.36	4.41 ± 3.27	133	144

This paper has been typeset from a TEX/LATEX file prepared by the author.